energies

Article

Comparative Study on Parameter Identification Methods for Dual-Polarization Lithium-Ion Equivalent Circuit Model

Theodoros Kalogiannis [1,2,*], Md Sazzad Hosen [1,2], Mohsen Akbarzadeh Sokkeh [1,2], Shovon Goutam [1,2], Joris Jaguemont [1,2], Lu Jin [3], Geng Qiao [3], Maitane Berecibar [1,2] and Joeri Van Mierlo [1,2]

1 ETEC Department & MOBI Research Group, Vrije Universiteit Brussel (VUB), Pleinlaan 2, 1050 Brussel, Belgium; Md.Sazzad.Hosen@vub.be (M.S.H.); Mohsen.Akbarzadeh.Sokkeh@vub.be (M.A.S.); Shovon.Goutam@vub.be (S.G); Joris.Jaguemont@vub.be (J.J.); Maitane.Berecibar@vub.be (M.B.); Joeri.van.mierlo@vub.be (J.V.M.);
2 Flanders Make, 3001 Heverlee, Belgium
3 Global Energy Interconnection Research Institute Europe GmbH, 10623 Berlin, Germany; Lu.Jin@geiri.eu (L.J.); Geng.Qiao@geiri.eu (G.Q.)
* Correspondence: Theodoros.Kalogiannis@vub.be

Received: 1 October 2019; Accepted: 22 October 2019; Published: 23 October 2019

Abstract: A lithium-ion battery cell's electrochemical performance can be obtained through a series of standardized experiments, and the optimal operation and monitoring is performed when a model of the Li-ions is generated and adopted. With discrete-time parameter identification processes, the electrical circuit models (ECM) of the cells are derived. Over their wide range, the dual-polarization (DP) ECM is proposed to characterize two prismatic cells with different anode electrodes. In most of the studies on battery modeling, attention is paid to the accuracy comparison of the various ECMs, usually for a certain Li-ion, whereas the parameter identification methods of the ECMs are rarely compared. Hence in this work, three different approaches are performed for a certain temperature throughout the whole SoC range of the cells for two different load profiles, suitable for light- and heavy-duty electromotive applications. Analytical equations, least-square-based methods, and heuristic algorithms used for model parameterization are compared in terms of voltage accuracy, robustness, and computational time. The influence of the ECMs' parameter variation on the voltage root mean square error (RMSE) is assessed as well with impedance spectroscopy in terms of Ohmic, internal, and total resistance comparisons. Li-ion cells are thoroughly electrically characterized and the following conclusions are drawn: (1) All methods are suitable for the modeling, giving a good agreement with the experimental data with less than 3% max voltage relative error and 30mV RMSE in most cases. (2) Particle swarm optimization (PSO) method is the best trade-off in terms of computational time, accuracy, and robustness. (3) Genetic algorithm (GA) lack of computational time compared to PSO and LS (4) The internal resistance behavior, investigated for the PSO, showed a positive correlation to the voltage error, depending on the chemistry and loading profile.

Keywords: lithium-ion characterization; ual-polarization equivalent circuit model; analytical equations; least-square; heuristic algorithm; EIS impedance spectroscopy; LTO; NMC

1. Introduction

Electrochemical energy storage cells with lithium have been gradually entering in all our society's power levels. Different types of commercially available Li-ion cells do exist presently with many more being under research [1,2]. Lithium-ion battery (Li-ion) cell's nominal performance in terms of volumetric (size) and gravimetric (weight) energies, specific power, operating voltage and charge/discharge loading capabilities depends on the formation of anode and cathode active material, electrolyte, separator, current collectors and cell's shape [3]. This composition characterizes electrically, thermally and mechanically the Li-ion cell with its nominal values at a certain temperature, also known as the beginning of life (BoL) state of the cell.

It is crucial to characterize, model and assess the cell's behavior at the BoL (off-line) and to adapt the identified parameters at various conditions and states (online) to enhance performance during operation. This is achieved by accurately obtaining the main parameters of the cells i.e., the impedance, capacity and open circuit voltage, and by deriving a suitable model for the microprocessors of the battery management system (BMS) that are designed to monitor and perform an optimal operation within a predefined safe-operation-area (SoA) and power limits [4]. The modeling of the Li-ions is achieved with one of the following methods [5,6]:

- Generic-based or data-based empirical models,
- Electrochemical impedance spectroscopy (EIS)-based models,
- Static and dynamic equivalent electrical circuit models (ECM) and
- Electrochemical and physics-based models.

The generic models are usually based on the Shepards equation [7], they are mathematical representations of the voltage usually with a low physical meaning. Hence they can be preferred for simple representation of the Li-ion batteries although they can be challenging for online parameter adaptation and state estimation.

The frequency domain models analyze the impedance of the cells in a wide frequency range with superimposed AC signal carried by a DC (charge or discharge) to investigate the overall working principle of the Li-ions. The linearity and time invariance of the system are achieved with the low AC power amplitude ranges of the experiment (mV or mA) which leaves aside however the current rate dependency on the cells [8,9]. Dealing with this, the non-linear Butler–Volmer equation (BVE) along with the Arrhenius relationship can give the charge-transferring temperature and current dependence of the cells [10], raising however questions on the accuracy and computation effort of solving on-board such non-linearities.

An electrochemical model has the highest fidelity, but it is a computational demanding representation of the working principles of the cells. This is accompanied with a huge number of parameters that must be identified and adapted to circumstances, which makes them so far inefficient for on-board applications.

A good compromise between physical representation of the cells and the fast modeling response is obtained with ECMs. They are further subdivided into static and dynamic modeling approaches. The former models represent the cells with simple polynomial equations suitable for constant charge/discharge representation. The latter can give a dynamic model that can be addressed to real-life loading cycling profiles. For either case, the ECMs are composed of lumped equivalent electrical elements that represent the working principles of battery to a certain degree. In one hand simple static models can be generated without any experimental characterization and can model accurate constant power profiles. Alternatively, dynamic ECMs require a series of electrical testing from which the lumped parameters are derived by applying parameter identification techniques. In most studies however, focus is laid on comparisons among the different modeling ECM approaches, nevertheless, to the best of our knowledge, the parametrization techniques are rarely compared under the framework of a certain chemistry and model, similarly stated by Lai et al. [11], in which however various ECMs are compared for several heuristic algorithms.

Furthermore, the low computational power of the BMS renders necessary not only to reduce the modeling parameters to the minimum necessity, but also to depict the electrochemical processes as accurately as possible. Regarding this, the second-order ECM, also known as the dual-polarization ECM is selected in this work to characterize the Li-ion cells. Three parametrization methods are investigated and compared for two different anode-based cells and two types of validation profiles are used to assess the identification results.

The generated ECMs in this work are compared for their robustness, computational effort and accuracy at an off-line modeling approach. Also, the power capability is estimated under charge and discharge of the cells, while impedance comparison among the proposed methods and EIS is taking place as a merit of evaluation on the physical accuracy of estimated parameters from the identification techniques.

This paper's overall motivation is seen in three parts:

- An experimental characterization and electrical modeling of the Li-ions with three different parameter identification methods,
- A comprehensive comparison among the parameter identification methods from previous studies,
- Analyses on the impedance behavior of the cells in time and frequency domain and estimation on the power capabilities of the cells.

The paper is organized as follows: the experimental setup as well as discussion of the Li-ions main characteristics and the experimental process are presented in Section 2, the proposed model development is analyzed in Section 3 and a comprehensive comparison on different parameter identification methods is performed in Section 4. Impedance results, comparisons over the methods and discussions are taking place in Section 5, whereas Section 6 concludes the paper.

2. Experimental Setup

2.1. Test Bench Description

Two commercial prismatic Li-ion cells are tested, suitable for either high-power or high-energy applications, one LTO and an NMC. Their shape and main characteristics are illustrated and compared in Figure 1, while Table 1 gathers the main electro-mechanical properties of the Li-ion cells.

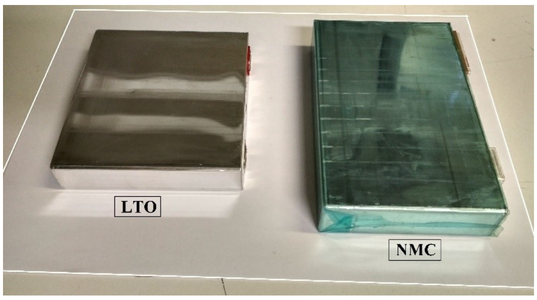

(a)

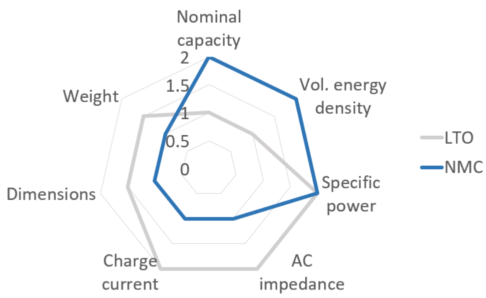

(b)

Figure 1. (**a**) Lithium-ion cells placed on a A4 paper. On the left lays the LTO and right is the NMC. (**b**) Lithium-ion cells nominal properties (datasheet) comparison at the BoL. *no*.#2 indicates a twice better behavior in absolute values.

Table 1. Manufacturing properties of the lithium-ion cells.

Main Characteristics	Value		Unit
Chemistry	LTO	NMC	[-]
Nominal voltage	2.3	3.65	[V]
Nominal capacity	23	43	[Ah]
End-of-charge maximum voltage	2.7	4.2	[V]
End-of-discharge cut-off voltage	1.5	3	[V]
Volumetric energy density	202	424	[Wh/L]
Specific energy density	96.1	186.8	[Wh/kg]
Specific power	>1200	>1200	[W/kg]
AC impedance (1 kHz)	0.6	1	[mOhms]
Recommended charge current rate (continuous)	4 C	1 C	[-]
10 s max charge C-rate	>8 C	3 C	[-]
Height	103	148	[mm]
Width	115	91	[mm]
Thickness	22	27.5	[mm]
Weight	0.550	0.840	[kg]

Figure 2 illustrates the test setup. Steel connectors are attached to the aluminum tabs with a spot-welding technique. Laser welding for aluminum-to-aluminum interconnection is also being investigated to compare the contact resistance and tensile force capabilities [12]. Cells are placed inside a temperature chamber to preserve 25 °C and they are connected to the PEC ACT0550 tester, capable of up to DC 5 V measurements with a ±0.005% accuracy.

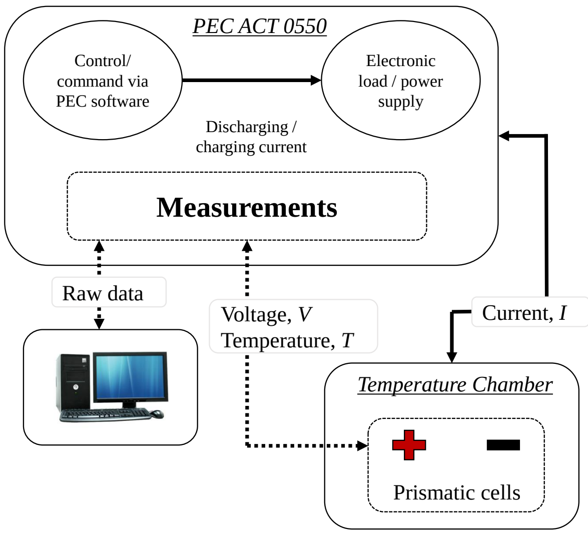

Figure 2. Topology of test bench and the battery cells during experiments [13].

It consists of equipment commonly found in a battery dedicated laboratory: Battery tester can charge/discharge and monitor cell's voltage, current and temperature, one K-type thermocouple for the surface of the cell and climate chamber to control the environmental temperature. Raw data in terms of voltage, current, power, energy, step, cycle and temperature.

2.2. Experimental Process

The methodology followed in this work to electrically characterize the Li-ion cells is summarized in the flow chart presented in Figure 3. In this section, the main characteristics of the cells and the methods employed for experimentally extracting the impedance are analyzed. A brief description on the several impedance measurement methods can be found also here [14].

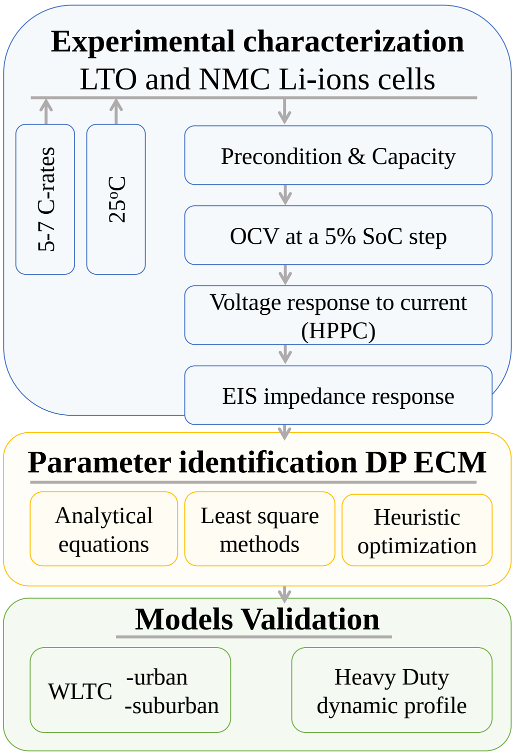

Figure 3. Division of this work in three main parts, the experimental characterization of the cells, the parameter identification process and the model validation.

2.2.1. Open Circuit Voltage Test

OCV test is performed to extract the voltage of the cells at no-loading and equilibrium state (V_{OC}). With a current rate of C/5 the batteries are fully charged and 5% discharging steps are followed until $V_{cut-off}$ to evaluate the V_{OC} after 3 h resting period, which takes place at each state of charge (SoC) step. Reverse procedure is followed for the charge OCV test. Regarding the relaxation of the cell voltage, it occurs due to the rapid discharge of the double layer capacitance as the ions move away from the electrode surface (at a range of msec) and the slower time-constant diffusions of the ion's redistribution within the liquid (electrolyte), until the concentration reaches equilibrium state and form the re-arrangement of atoms within the solid materials (electrodes). To incorporate for the slow diffusion processes of the cells, it is recorded that after 240 min the double layer capacitance and the diffusion processes in solid and liquid do not significantly change the impedance and the voltage error lays between measurement noise regardless cell type and chemistry, whereas after approximately 900 min of relaxation time, equilibrium is reached [15,16]. Figure 4 shows the measured V_{OC} during charge and discharge of the cells.

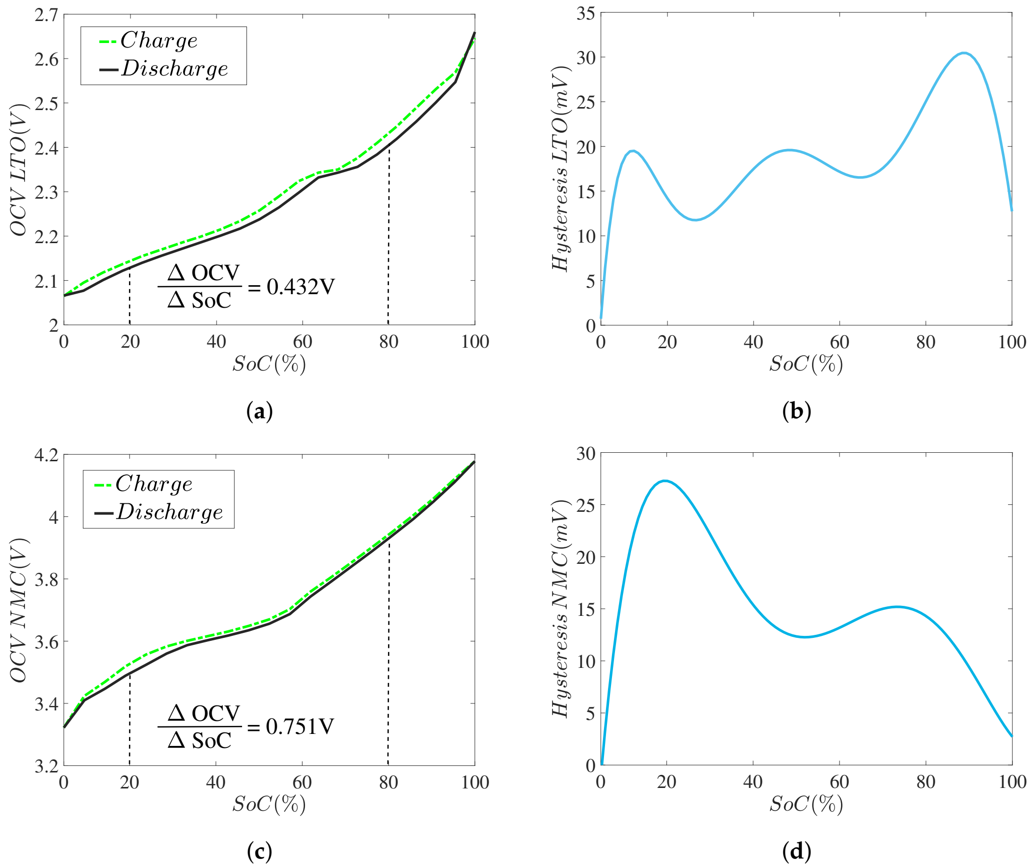

Figure 4. Open circuit voltage of (**a**) LTO cell and (**c**) NMC cell during charge and discharge. Hysteresis effect on both cells in (**b**) and (**d**) respectively.

OCV curves are fitted with an nth order polynomial as $V_{OC} = f(SoC) = \alpha_{n^{th}} SoC^{n^{th}} + \cdots + \alpha_1 SoC + a_0$ or adopted with look-up tables. It is observed that V_{OC} measured during charge is slightly higher for both chemistries. This, SoC dependent phenomenon, can arise from the internal resistance increase in the electrode at the edges of the charge/discharge and it is referred in the literature as hysteresis [17]. It is observed that the hysteresis behavior changes with the chemistry; however, it is more significant for the higher non-linear regions between 0–20% and 80–100% of the SoC. Accordingly, for the Li-ion that pose such relative low hysteresis levels a direct modeling approach is adopted [18]. Usually, the hysteresis branch on the modeling is proposed for chemistries that show a greater effect, such as in LFP chemistry, in the ranges of 50 mV and above. Regarding this, authors in [19] suggest the one-RC model with hysteresis that comes without an extra increase in complexity, as a better trade-off of such chemistry modeling approach.

Nevertheless, a brief comparison on the cells OCV shows a faster voltage increase of the NMC cell ($\Delta OCV/\Delta SoC$) at the slow dynamic area ($20\% < SoC < 80\%$) which, in addition to inadequate relaxation time, can affect the OCV-based SoC estimation methods [20]. At such cases, a structured ECM that embodies the Li-ion's hysteresis behavior is a requirement.

2.2.2. Voltage Response to Current Test

The voltage response to several current rates is investigated at the same temperature as the OCV test. A CCCV charge profile is applied to the cells to reach the 100% SoC, and it is followed by discharge pulses with C/5 at a 5% SoC step, until the voltage cut-off limit is reached. Right after each 5% SoC drop, five (for NMC) or 7 (for LTO) current pulses at various rates, with a $\Delta t = 10$ s duration are performed before the cells are rest for a relaxation time, similar to OCV test. The current pulses with different amplitudes are applied at both charge and discharge directions with one-minute rest in-between.

2.2.3. Impedance Response to Frequency Test

Li-ion characterization technique through current pulse (HPPC) results in discrete-time-dependent impedance measurements. However, realization of electrochemical properties and phenomena such as the impedance growth during intercalation and de-intercalation of lithium charge and discharge process cannot be investigated with this method. On the other side, EIS is a common method for this purpose where the key power limiting factors such as electrolyte conductivity, solid-electrolyte interface (SEI) growth and the charge-transfer resistance behaviors can be analyzed with an small AC excitation signal [21]. It is a method extensively used over the years in battery characterization [22] and battery ageing [23,24]. Here, a potentiostatic EIS is performed on both cells with BioLogic MPG-205 equipment and the impedance spectra is generated by imposing an AC voltage impulse from 10 kHz to 5 mHz frequency range and at controlled ambient temperature of 25 °C and 4.3 mV amplitude. Figure 5 shows the plotted Nyquist curve for the Li-ion cells at five different SoCs (0%, 20%, 50%, 80% and 100%) to illustrate the evolution of imaginary against the real impedance.

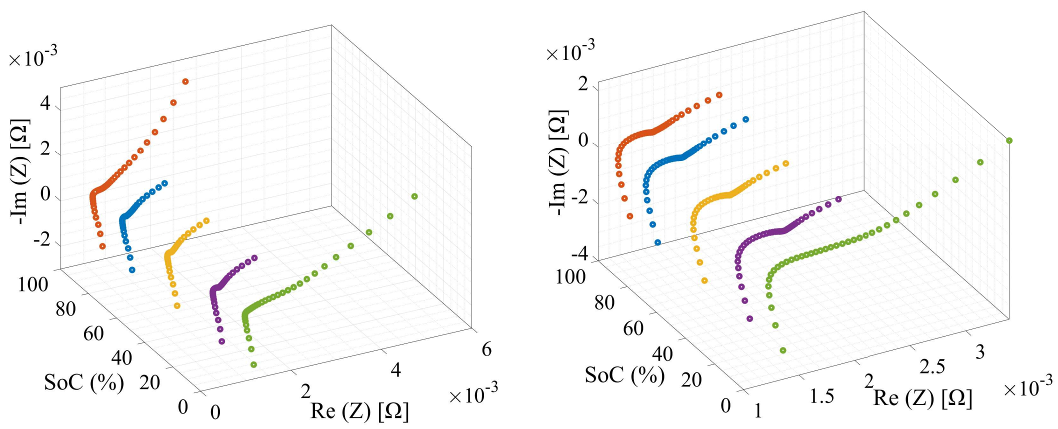

(**a**) (**b**)

Figure 5. Nyquist plots of (**a**) LTO and (**b**) NMC, over the different SoCs.

Ohmic resistance is obtained at the intersection of the real and the imaginary axis. As with [25] and depending on the chemical composition of the cells, the curve is shifted here towards right and upwards with the decreasing SoC indicating the increment on the Ohmic resistance as the SoC is decreased. From the generation of the EIS-based models, the DC offset that creates the charge-transfer impedance to current dependency cannot be incorporated, which makes the ECM inefficient for dynamic loading profiles. This challenge is addressed, and will be further analyzed in following section, with the Butler-Volmer equation (BVE).

2.2.4. Capacity Test

During charge and discharge at different current rates, the capacities of Li-ion cells differentiate from the nominal values in a reverse proportional rate to the current as described by Peukert's law [26], whereas they are also follow an Arrhenius temperature dependency [27]. This study focuses on 25 °C for which the capacities values of both cells during charge and discharge, as well as approximation of the Coulombic efficiency $\eta = AhDischarge/AhCharge$ are calculated. In the case of inadequate relaxation period after the CCCV charge an increased discharged capacity can be measured and η is set to 1. Also, a slightly higher capacity of the cells can be observed while increasing the C-rates at a certain temperature (usually low) due to the proportional enhancement of the charge-transfer kinetics occurring from the increased (self-heating) temperature. To cope with this, cells are placed in a climate chamber that actively monitor and maintain temperature as close as possible to the predefined 25 °C. Capacities of the cells are shown in Table 2.

Table 2. Charge and discharge capacities of the lithium-ion cells at 25 °C.

Value	LTO					NMC					Unit
C-rate	C/3	C/2	1C	2C	4C	C/3	C/2	1C	1.5C	2C	[-]
Charge Capacity	23.2	23.1	23	23	22.9	44.9	44.9	44.8	44.7	44.7	[Ah]
Discharge Capacity	23.6	23.3	23.1	23	22.8	45.3	45.2	45	44.9	44.8	

3. Model Development

3.1. In Discrete-Time Domain

The model that is employed in this work is the dual-polarization ECM which refers to the second-order RC circuit as shown in Figure 6. It represents the time-dependent polarization processes taking place during charge/discharge, the relaxation effect and the equilibrium open circuit V_{OC} in the battery cells. At a current passage, the terminal voltage V_{batt} diverges from the V_{OC} due to material resistivity, electrochemical reactions and diffusion processes [28].

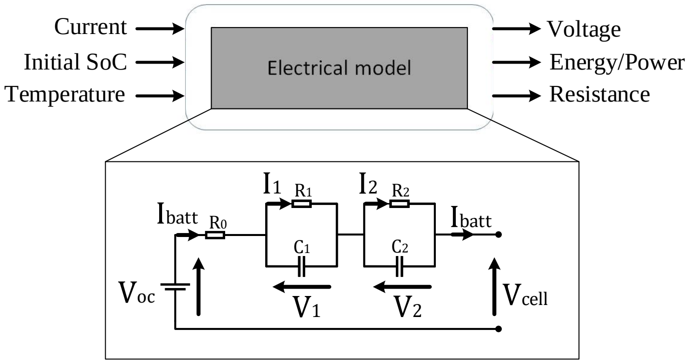

Figure 6. Dual-polarization electrical equivalent modeling approach of the Li-ion prismatic cells. Model input is the current, the initial SoC and the temperature. Model output is the voltage response, resistances and energy/power capability of cells.

The ECM considers the load demand, the initial SoC of the cells and the temperature as inputs in order to estimate the terminal voltage and the states of the Li-ion cells which are described by Equation (1):

$$\begin{aligned} V_{batt} &= V_{oc} - V_1 - V_2 - R_0\, I_{batt} \\ \dot{V_1} &= -\frac{1}{R_1\, C_1}\, V_1 + \frac{1}{C_1}\, I_{batt} \\ \dot{V_2} &= -\frac{1}{R_2\, C_2}\, V_2 + \frac{1}{C_2}\, I_{batt} \end{aligned} \tag{1}$$

where V_{oc} is the OCV obtained from the experiment, R_0 is Ohmic resistance, R_1 and R_2 represent the activation (electrochemical) and the concentration polarization respectively (mΩ) with the capacitances (C_1 and C_2 in kF) as to relate the voltage drops across them (V_1 and V_2 in mV) with the two different time-constant. The former, activation polarization V_1 is associated with the charge-transfer and the SEI layer build up resistance. The latter accounts a concentration gradient build-up taking place at current flow or during vice-versa during relaxation, represented by V_2. I_{batt} is the current flow through the battery cells (Amps) with a sampling period of $T_{sample} = 0.01$ s and it is considered negative for charge.

Since the impedance is dependent on the SoC, a function for this purpose is integrated in the DP ECM. Generally, the SoC of cells can be estimated with OCV(SoC)-based method [29,30], with power electronics such as online EIS measurement [31,32], model-based-estimation and machine learning algorithms, and Ah(Coulomb)-counting, as it thoughtfully discussed in previous studies [33–36]. Challenges with certain chemistries can rise, as for LFP's low $\Delta OCV/\Delta SoC$ at the slow dynamic area and its hysteresis effect makes OCV (SoC)-based methods not optimal [37,38], whereas EIS-based measurements lack accuracy through ageing and the estimations are highly influenced from chemistry and experimental conditions [39]. Also, due to overload on computational complexity and memory storage or lack of accuracy, most implementation are to not suitable for on-board applications. However, certain model-based methods and the Ah-counting are proven more relevant for this purpose.

More in precise, the model-based estimation with adaptive Kalman and particle filters or observers and fuzzy logic [40–42] or machine learning algorithms such as artificial neural networks (ANN) [43,44] and support vector machines (SVM) [45] are typically used for on-board implementation, taking into account their increased computational and memory requirements. On the other hand, the SoC estimation from Ah-counting [46] depends on the accuracy (sampling precision and frequency) of the current sensors and the initialization of the cell's capacity. It usually gives accurate results, which also relies on the initial and re-calibrated (to avoid error accumulation) SoC after dynamic load profiles [47]. This low-cost estimation method is used in this work as well, according to Equation (2).

$$SoC(t) = SoC_0 - \frac{\eta}{C_n} \int i(t)\, dt \tag{2}$$

where SoC_0 is the initial state of charge, η is the Coulombic efficiency of the cell at the certain C-rates, $i(t)$ is the instantaneous current through the cell and C_n is the initial capacity ($Asec \cdot Ts$ = discrete sampling period) as a function of temperature and current rate.

Besides the ECM parameters, the total cell's resistance incorporates both the Ohmic and polarizations and is considered to be the DC resistance of the Li-ion that can be extracted according to Ohm's law from the measured voltage drop at a current pulse as in Equation (3):

$$\begin{aligned} R_{DC,pulse}|_{\Delta t} &= \frac{\Delta V_{pulse}}{I_{pulse,max}} \\ \Delta V_{pulse}|_{\Delta t} &= V_{max,pulse} - V_{OC,pulse} \end{aligned} \tag{3}$$

where ΔV_{pulse} is the overpotential between the terminal voltage $V_{max,pulse}$ and the $V_{OC,pulse}$ of the current pulse. This resistance is a modeling assumption that represents the overall impedance of the cells during a current excitation which is practical for on-board estimation of the available source or sink power capability of the cells P_{pulse}, and also the limitation on rate of current $I_{pulse,max}$ that can be drawn or fed on either charge or discharge direction over a short period of Δt. They can be estimated according to Equation (4) [48]:

$$P_{pulse}|_{\Delta t} = \frac{\Delta V_{pulse} \cdot V_{max,pulse}}{R_{DC,pulse}} \tag{4}$$

The power capability is inverse dependent on the R_{DC} of the battery cells and follows the overpotential ΔV_{pulse} build-up during the pulse. As a result, it is highly influenced from the C-rates, the operating temperature and the current pulse length period, as well as the SoC of the cells throughout ageing and their chemistry [49]. Consequently, P_{pulse} is assessed here for three C-rates (0.33 C, 1 C and 2 C-NMC or 3 C-LTO) and at three SoCs (20%, 50% and 80%), for three different pulse times Δt = 2 s, 10 s and 20 s at 25 °C and BoL. The generated power losses at the respective states can be simply calculated by $P_{loss} = I^2_{pulse} R_{DC,pulse}$ [in the range of a few Watts].

3.2. In Frequency Domain

The impedance analysis in time domain is a combined effect of resistance and overpotential at a current excitation. To get a clear view on the individual generated resistances and losses, the proposed equivalent circuit illustrated in Figure 7 is selected. EIS can effectively separate the losses with different time constants (Ohmic, solid-electrolyte interface (SEI), charge-transfer, diffusion), evolving at frequencies between several kHz to a few mHz range [50]. Depending on the chemistry and state of health, the first semi-circle is related to the SEI layer of the anode. Nevertheless, in this work a single semi-circle associated with the double layer capacity and charge-transfer resistance on the electrodes is observed and modeled accordingly, assuming the impact of SEI formation negligible and with similar time-constant.

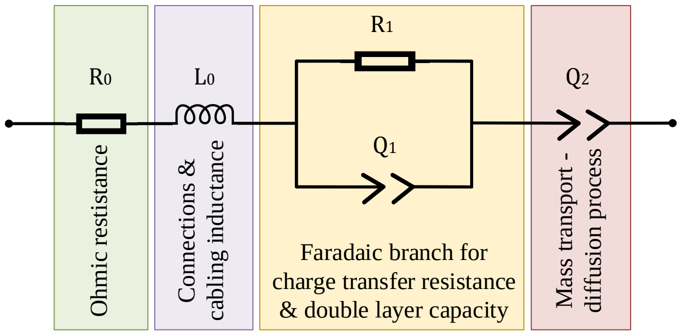

Figure 7. Topology of EIS proposed equivalent model.

The key elements in this modified Randles circuit model are L_0 which represents the cabling and connection inductance and R_0 the Ohmic resistance of the battery cell generated from the material composition conductivity. They are observed in the highest frequency ranges of the EIS spectrum, characterized by the materials and the surface geometry, where in our case deviate form 10^4 to 10^2 Hz. Also, the parallel branch R_1 with the constant phase element (CPE) Q_1 which combines the kinetics impedance related to the electrochemical charge-transfer and double layer, it takes place in the range of 10^3 to 10^0 Hz [51,52]. Lastly, a second CPE Q_2 related to diffusion process and the mass transportation is modeled which is considered at low frequencies and time-constant in the range of several seconds to minutes [53,54]. These parameters are obtained from EC-Lab®fitting software based on Equation (5) [55]

$$Z_{EIS} = j\omega L_0 + R_0 + \frac{1}{R_1^{-1} + (j\omega)^{\xi_1} Q_1} + \frac{1}{(j\omega)^{\xi_2} Q_2} \tag{5}$$

where Z_{EIS} is the impedance of the ECM and $\frac{1}{(j\omega)^{\xi_{1,2}} Q_{1,2}}$ is the impedance of the CPE elements with a depression factor $0 \leq \xi_i \leq 1$ on the Nyquist plot (0 = resistor, 1 = capacitor with ideal semi-circle of R//C).

The proposed EIS equivalent model gives a good fit with experimental data which can be seen in Figure 8 for LTO and NMC cell, respectively. According to previous studies various modeling representations of Li-ions in frequency domain are proposed by adding either extra parallel branches of R//CPE elements [54,56] or Warburg element [57] in order to approximate more accurate the electrochemical reactions taking place in the whole frequency spectra, with a trade-off between modeling simplicity and accuracy [22]. In this work, as also explained in next section, the proposed model topology of Figure 7 is selected, as it shows good agreement to the experimental data with the minimum required lumped elements. The values associated with the EIS model fittings are shown in Table 3 for all the SoC steps. The corresponding modeling error ($Z_{EIS} - Z_{model}$) stays below 1.52 $\times 10^{-5}$ for most cases, generated from the EC-Lab®fitting software.

Table 3. Frequency domain impedance model parameters for both prismatic battery cells at 25 °C and five SoC steps.

Parameter	LTO					NMC					Unit
SoC	**100**	**80**	**50**	**20**	**0**	**100**	**80**	**50**	**20**	**0**	**[%]**
R0	0.709	0.714	0.782	0.883	0.953	1.25	1.26	1.306	1.31	1.33	[mΩ]
R1	0.175	0.136	0.122	0.123	0.179	0.359	0.35	0.358	0.434	0.963	[mΩ]
Q1	46.4	283	169.1	43.27	302.8	19.34	18.23	15.45	21.14	176.1	[$\Omega^{-1} \times s^{\tilde{\xi}}$]
Q2	847.7	6987	8449	7209	883.3	9198	8822	10,970	10,726	3662	[$\Omega^{-1} \times s^{\xi}$]

The simulated and experimental data comparison was done at 50% SoC and at room temperature. The impedance parameters of R_0 can be extracted from the fitted curves and R_1 can be calculated from the plotted curves semi-circle to represent charge-transfer resistance between electrolyte and active materials [58].

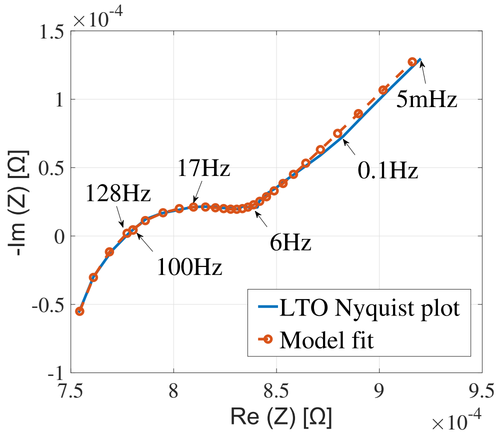

(**a**)

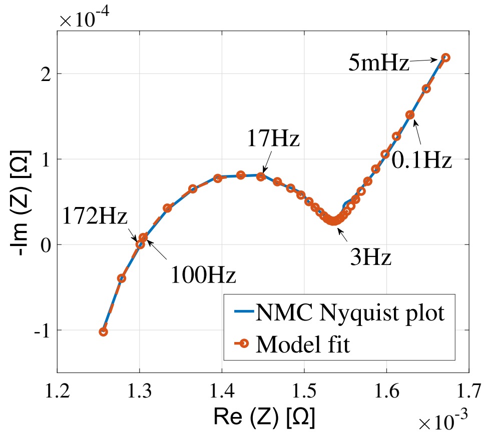

(**b**)

Figure 8. Nyquist plots and the fitted model of (**a**) LTO and (**b**) NMC battery cells at 50% SoC.

3.2.1. Ohmic Resistance

Ohmic resistance varies during charge/discharge due to the materials composition and their conductivity properties. It is strongly dependent on the ionic conductivity of the electrolyte [59,60], the electric resistance of the electrode, tabs and current collectors and their interfacial resistance [61]. It can change over temperature, ageing and SoC fluctuations, while it is mostly independent on the current's amplitude and the relaxation time. It is observed that impedance obtained from EIS at the $f_{sample} = 100$ Hz deviates from EIS R_0 (at the intersection of the curve with zero imaginary axis) at less than 0.06 mΩ. More in precise, the intersection of real to imaginary part takes place accordingly at frequencies $f_{intersection}$ = 128 Hz and 172 Hz for LTO and NMC. The deviation has a positive correlation to the $\Delta f = f_{intersection} - f_{sample}$ whereas here, either point is considered to have a minor effect on the determination of the R_0, as also discussed in the voltage to current response section. Hence, both Ohmic resistances obtained are used as a benchmark to compare the Ohmic resistance acquired from time-domain modeling at the same sampling frequency. It should be noted here that determining pure Ohmic resistance requires a very fast sampling capacity. In our case, since it is close to the sampling frequency the error of the HPPC and the EIS can be low, but other chemistries that the Ohmic is generated at the range of 0.5 kHz (such as LFP in [23]), its measurement from HPPC is impractical.

3.2.2. Charge-Transfer and Total Resistance

An electric field applied to the current collectors results in a current density described by the BVE, as a function of the electrochemical charge-transfer overvoltage during redox reactions at the electrodes. On the contrary to the Ohmic resistance, the Faradaic branch elements $R_1//Q_1$ are highly dependent on current density but also at SoC, temperature and ageing. During the first instances at a charge/discharge pulse for the high frequencies, the double layer capacitor impedance acts as a short circuit and it is quickly charged. Consequently, at lower frequencies it effectively behaves as an open circuit and the whole current is flowing through the charge-transfer reaction. A superimposed DC current EIS technique can be used to fit and quantify the charge-transfer R_1 resistance [62]. Alternatively, the total resistance can be used, obtained either at the end of the EIS frequency spectrum 5 mHz, or from the pulse test if both the linear Ohmic resistance overvoltage and the logarithmic electrochemical are considered. The modified BVE can be used as in Equation (6), only if the mass transport is neglected at cases with lower than 5 s pulse currents [3,63,64]:

$$\begin{aligned} V_{oc} - V_{batt} &= R_0 I_{batt} + V_1 + V_2 \Rightarrow \\ V_{oc} - V_{batt} &= \Delta V_{DC} \\ I = I_0 \cdot \{\exp(&\frac{\alpha_{anodic} nF}{RT}\Delta V_{DC}) - \exp(\frac{-\alpha_{cathodic} nF}{RT}\Delta V_{DC})\} \end{aligned} \tag{6}$$

where n, F, R, T are constants: n is the number of electrons involved in the reaction per molecule of the active material, F the Faraday constant, R the general gas constant, T the absolute temperature in Kelvin [65]. By performing current pulses technique and using a simple NLS fitting of Equation (6) to the results, missing information on the α, I_0 constants can be found and the $R_{DC} = f(I)$ be estimated. A thorough investigation on the non-linearities of the symmetry factors α and the exchange current density I_0 can be found in [64] for LTO cells, signifying their evolution over various states and temperatures. Another approach by Zhu et al. in [66], approximates both the non-linear dependency on current and temperature of the modeled resistances obtained from a 30 s HPPC test, where they propose an electro-thermal model to predict power at low temperatures.

If V_1 is used instead of the DC overpotential, the pulse technique is not required and the charge-transfer resistance $R_1 = f(I)$ dependency on the current can be estimated by making certain simplifications on the BVE, as analytically discussed in [65]. In this regards, assumptions are made on the symmetry factor for both redox reaction rates depending the desired complexity level on the current dependency approximation, i.e., either symmetric kinetics $\alpha_{anodic} = \alpha_{cathodic} = 0.5$, $\alpha_{anodic} + \alpha_{cathodic} = 1$ [67] are assumed i.e., the reaction processes are at the same speed, or the influence of voltage drop on small currents is negligible according to Tafel equation and the cathodic part of the BVE could then be neglected [68].

3.2.3. Diffusion Resistance

At frequencies between 5 Hz–5 mHz for the Li-ions under testing here, the diffusion processes caused by the ion concentration at the location of the charge-transfer creates a diffusion overvoltage which is generally described by Fick's law [69], and is modeled here with the CPE Q_2. The time-constant that describe the diffusion processes depend on the electrode geometry, temperature and electrolyte ion concentration [50].

Diffusion overvoltage is becoming more pronounced for high rated excitation currents with periods more than $\Delta t = 5$ s. It is the main reason for decreased capacity of the Li-ions over a full discharge cycle at increased current rates and the proportionally increased Joule losses. This is an effect of the ions that cannot be diffused fast enough in the place of charge-transfer and create a high ion concentration c at the electrode-electrolyte interfaces which creates high overpotential V_2 with the aforementioned results. Equation (7) describes this correlation where c_0 is the equilibrium concentration [28]

$$V_2 = \frac{R \cdot T}{n \cdot F} \cdot ln(\frac{c}{c_0}) \tag{7}$$

The working principle of the EIS brings challenges in the identification of the slow time-constant diffusion processes within liquid and solid [70], while a Warburg element may represent one out of three possible diffusion processes [50]. Other empirical approaches have proposed to model accurately and temperature depending the diffusion resistance with adding a proportional to the square root of time resistive element, dependent as well on the open circuit voltage V_{OC}, instead of CPEs [71]. In either case, excitation signals are applied to the Li-ion for several mHz to avoid close to DC excitations and prevent changes over the SoC or exacerbated ageing effects. Addressing to this, authors in [72], propose a method to extract the electrolyte and solid-state diffusion overpotential from the HPPC pulse test for much lower frequencies. They performed it by suppling a 6min pulse and a 3h open load resting period, subtracting the high-frequency contribution obtained from the EIS, to the relaxation overvoltage after the current is switched off, and subsequently estimate the diffusion equivalent resistance after the applied potential is released.

4. Review of the Most Frequently Used Identification Methods

The identification methods are divided in the literature into three main categories, according to the characterization processes of cells that is followed. First, EIS group that characterizes the equivalent impedance in the frequency domain. Second, impedance characterization generated from the electrical standardized test and third, electrochemical models which can be the most accurate but least computationally efficient for on-board applications [73]. in this work the third modeling approach is not investigated, where the parameter identification methods for the rest are addressed by one of the following categories:

- Analytical equations,
- Least-square-based methods,
- Heuristic optimization algorithms,
- Impedance spectroscopy methods and
- Kalman or adaptive filters and observer-based methods.

These methods are used for parameter identification and can be applied for on-board model-based state estimation and parameter tracking. In Figure 9 the parameter identification approaches are summarized.

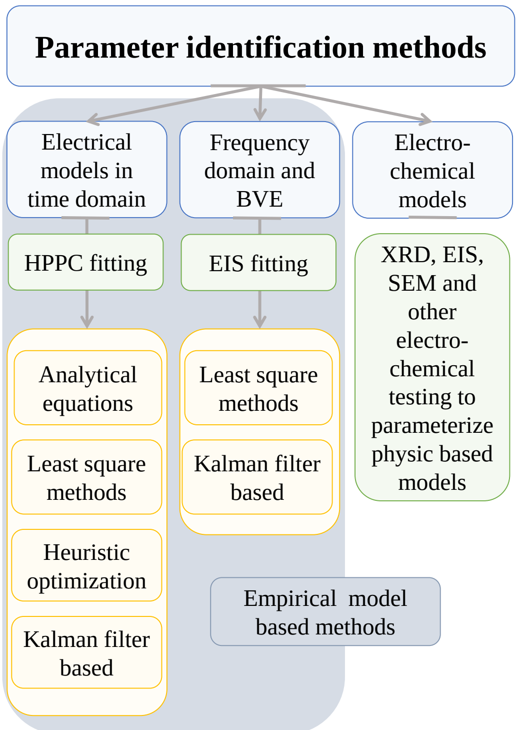

Figure 9. Parameter identification methods.

The empirical model-based methods that are obtained from experimental observations and mathematical representations are discussed. Also, Table 4 gathers several references with the aforementioned parameter identification methods.

4.1. Parameter Extraction with Analytical Equations

Modeling a Li-ion in the time domain (TD) uses the differential equations that describe the ECM as in Equation (1). It is a straightforward mathematical approach that identifies the resistances and the capacitances of the nth order ECM from the HPPC based on Equation (8).

$$\begin{aligned} R_n &= \frac{\Delta V|_j^k}{I_k(1-\mathrm{e}^{-\frac{t|_j^k}{\tau_n}})},\ C_n = \frac{\tau_n}{R_n} \\ \tau_n &= \frac{\Delta t|_j^k}{logV_j - logV_k},\ x|_j^k = x_k - x_j \end{aligned} \tag{8}$$

where R_n,C_n and τ_n are lumped parameters of the selected nth order ECM obtained from HPPC at the discrete pulse time of $\Delta t|_j^k$. R_0 is calculated similarly to the DR resistance (Equation (3)) for the Ohmic region. Defining the starting and ending points j, k of the respective Ohmic and polarizations areas is the main challenge. Waag et al. in [63] used —an application specific— linear approach of the voltage response at a 10 s current excitation to decouple the Ohmic and the electrochemical to the concentration polarization overpotential after a 5 s period. On the other side, it usually appears as an arbitrary process, sample/time-dependent and defined from observations on the voltage pulse behavior [74–77]. As a general rule, the concentration polarization voltage response reaches steady state at approximately four to five-time constants $\Delta t = 5RC$ after switching off the current.

In [75] the time-domain DP is analyzed based on the power profile of a heavy-duty underground mining load-haul-dump (LHD) loader with a 20 kW average power per cycle. A battery pack is constructed with seven 40 Ah NMC cells in series and the DP is parameterized with TD analytical equations. A mean absolute percentage error (MAPE) of less than is 0.2% is seen signifying the applicability of the method for heavy-duty modules as well.

In Figure 10, the regions at the HPPC are chosen according to EIS, where Ohmic is considered on the $f_{hppc} = 100$ Hz sampling frequency as previously discussed ($j = 1, k = 2$), the activation and concentration polarization regions are defined at the theoretically first sample of a $f_{hppc}/6 = 17$ Hz and a $f_{hppc}/1000 = 0.1$ Hz sampling frequencies respectively, with the corresponding sampling points at $j = 2, 6$ and $k = 6, 1000$ respectively. The 17 Hz value is as close as possible to the local minimum frequency f_{min} of the semi-circle for both cells, which defines in the EIS impedance characterization, the time-constant $\tau = 1/2\pi f_{min}$ of the semi-circle. The latter value of 0.1 Hz is the last point of the HPPC 10sec pulse, which fall inside the low-frequency diffusion area of the EIS.

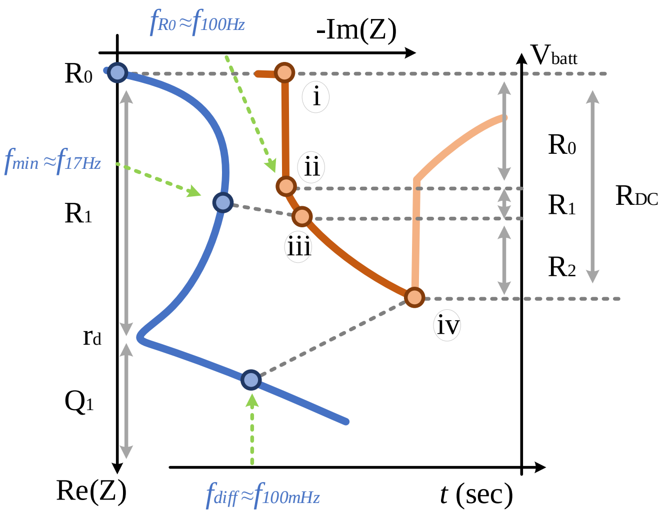

Figure 10. Approximation of the time intervals for the polarization instances based on the frequency domain EIS.

4.2. Parameter Extraction with Least-Square Methods

The second group of the parameter identification includes the least-square methods (LS) which are based on non-linear curve fitting of the experimental to the modeling data set by minimizing the sum of squared residuals. Several versions of LS methods are structured upon their methodology: the recursive least-square (RLS) with or without forgetting factor to adapt their actual changes over the lifetime, the weighted recursive least-square (WRLS) to weight recent data more than old, or the weighted recursive least-quadratic-squares (WRLQS) and others can be found in [68,78–81]. Recursive LS methods have shown fast-computing capability with high accuracy and low data storage requirements, capable of surpassing the computational limitations for a BMS integration.

In this work, since the Ah-counting is proposed for SoC estimation and the cells are tested at the BoL aiming to assess the efficiency of various parameterization methods, the trust-region-reflective non-linear least-square algorithm is employed, which however is susceptible to divergence problems by getting trapped to local minima when the initial values are not precisely defined [82,83]. A straightforward calculation based on the discrete TD equations is performed to set the initial values of the R,C elements according to Equation (8). The rest values, are optimized by minimizing the objective function as Equation (9):

$$F_{obj} = \sum_{t_i=1}^{\Delta t} (V_{batt,t_i} - V'_{batt}(t_i))^2, i \in [1, s] \tag{9}$$

where V_{batt,t_i} is obtained from HPPC response and $V'_{batt}(t_i)$ is the estimated value defined in Equation (1) for a total s = 1000 samples. More details on the LS algorithm can be found in [84] and for the current flow through the polarization resistance in [85].

In previous studies, NLS method is implemented to characterize the DP model impedance of a A123 14 Ah LFP battery cell and to obtain the SoC with a proposed EKF [86]. Various high current pulses are also implemented to assess the internal resistance's behavior over a wide current range, giving a max voltage RMSE < 12 mV with dynamic stress test (DST) profile. Wang et al. in [87] perform another modeling comparison which reveals that the DP model characterized with NLS performs better for SoC estimation with a combined EKF-Ah method, compared to the Thevenin or PNGV ECMs. This model show a lower SoC estimation error validated with DST and constant current discharge profiles with a voltage RMSE = 11 mV.

Recursive LS methods are used to identify the 1st order impedance of a 940 mAh NMC Li-ion cell over a certain cycling lifespan in [88]. The authors use a second-order EKF, which is designed for state estimation and the model is validated with DST and federal urban driving schedule (FUDS) giving a voltage mean relative error (MRE) lower than 2% for the BoL with an increasing trend over the end of life at about 10%.

To cope with the slow change of the parameters that the RLS alone cannot instantaneously capture, authors in [89] use an optimal forgetting factor that tends to 'forget' the older values on the parameter estimation and give to latest data more influence, usually to incorporate temperature and ageing effects on the cells. In this regard, seven ECMs compete for the most accurate modeling approach, in terms of voltage MRE and RMSE accuracy. The comparison is implemented based on a 10 Ah LFP battery cell and the models are validated with DST and a FUDS showing the lowest absolute and RMS errors for the DP model. The RLS with an optimal forgetting factor is also employed in [90] where the SoC estimation is compared and validated for three different Li-ions. Also, here, the DP model is compared with the Thevenin and is found to have lower voltage and SoC inaccuracies.

To further investigate the computational accuracy of the different LS methods on the Li-ion cells, reference [91] proposed an RLS method that decouples the slow and high dynamic areas (for low and higher $\Delta OCV/\Delta SoC$ respectively) of the OCV by employing linear low and high pass filters. A better performance has been achieved compared to the conventional WRLS method. Following this approach, authors in [81] investigate the accuracy of the DP model of an 18650 cylindrical NCA cell based on a decoupled WRLS method. They separate the slow and fast dynamic area and the DP model impedance is created based on the two different observations in time domain. It is seen that the model shows a better performance compared to simple RLS-based method, whereas also, the benefit on the SoC estimation accuracy with the DWRLS method is underlined, without any need for filtering or observers which could potentially decrease the computational efficiency.

As a last remark, LS methods have been used in a multi-cell topology for determining the highest impedance among the cells as well. This is achieved in [92] where the RLS method is used to obtain the impedance and the OCV information of each cell and to determine the states and power capability of a battery pack.

4.3. Parameter Extraction with Heuristic Optimization

An alternative approach on the identification methods that requires the problem's convexity and appears more suitable for high non-linear and discontinuous functions is based on the heuristic algorithms [93]. Several algorithms have been proposed in the literature, depending on their methodology: evolution-, physics- and swarm-based methods, which respectively include the genetic algorithms (GA), simulated annealing algorithm (SA), particle swarm (PSO), ant colony (ACO), firefly algorithm (FA), grey wolf (GWO), whale optimization algorithm (WOA) and the multi-verse cosmology-based (MVO) optimizations. A comparative study for such methods on various Li-ion ECMs is performed in [11], while characterizing a 32.5 Ah NMC pouch cell. The authors proposed a relationship in the model-to-parameterization approach based on the model's efficiency and the algorithm's computational time and accuracy. For the DP model, PSO, GA and then FA showed the highest robustness, whereas PSO requires by far the lowest computation time to converge. It is also the most accurate whereas authors suggest FA for higher-order ECMs due to its superior identification capacity, lacking though on the computational time.

The heuristic algorithms have been used depending the study, mostly aiming on the ECM comparison and assessment and not to the identification efficiency. The GA is used in [85] to analyze for an LMO cells with five different ECMs. A DST is performed to estimate the voltage mean absolute error (MAE) of the proposed models, where it is shown that the DP shows the lowest values. Also, in [94] authors examine 12 ECMs of an NMC and LFP with low capacity cylindrical cells. The selected models cover a wide range of ECMs from simple polynomial representation to enhanced self-correcting (ESC) models with two and four states of low-pass filtering, and up to third order with or without hysteresis block. The parametrization of the proposed ECMs is implemented with a multi-swarm particle swarm optimization (MPSO), another heuristic algorithm similar to PSO but modified to improve its global search capability [95]. It is found that the Thevenin ECM with hysteresis (LFP) and without (NMC) can provide the optimal results in terms of voltage ME and RMSE. Also, in [96], authors assess the performance of GA parameterization method on 11 ECMs. The models are checked for accuracy and robustness in terms of parameter fluctuations and inaccuracies of the SoC estimation. The authors showed that increasing the number of equivalent models by more than two brings no benefits as the complexity during parameterization increases along with the estimation error, whereas the EKF cannot overcome this modeling weakness which results in the SoC error becoming increasingly large when using a high-order RC model. Lastly, in [97], authors use a GA to investigate four different modeling approaches of an LFP 10 Ah cell. A crude approximation of the LFP's dynamics is made with a mathematical combined model, a better performance is achieved with a 2nd order ECM, whereas a single-particle model and a data-driven with support vector machine shown the best accuracy but with significantly increased required computational time.

The GA has been preferred in this field of research where structural details of the GA algorithm implementation can be found in [98–100]. Nevertheless, PSO compared to GA is faster since it involves no mutation or crossover functions and usually outperforms GA for unconstrained non-linear problems such as Li-ion ECMs [101]. It is being preferred for higher complexity studies such as in identification of certain electrochemical parameters that can significantly change over ageing [102]. Other research use hybrid GA-PSO [103], non-linear regression with PSO [104], and coevolutionary CPSO [105] to enhance the optimization process on state and parameter estimation. The addressed challenges with heuristic methods include the number of parameters that they have to optimize, the respective computational time and memory requirement, the construction of a solid objective function and the robustness of such probabilistic methods within a stable accuracy limit as the results are obtained from a random population, generations and observations [106]. On the other hand they do not require initialization of the parameters and multi-objective functions can be defined to enhance the accuracy and the computational time on problems with several conflicting criteria such as temperature, current rates, ageing etc. [107,108]. Hence in this work, GA and PSO are compared to assess the speed, the robustness and the accuracy on two Li-ions with different characteristics. Since the experiments are held in the BoL and 25 °C a single-objective approach is proposed as in [109]. According to literature research, the optimization criterion to define the optimal value can be set with either the mean or their square residual, or the RMS minimization. In this work, a brief comparison of several fitness approaches has shown that the execution time inversely changes with their complexity. Increasing the modeling accuracy has been the merit of selection in this study, and the objective function is hence formulated as the minimization of the total absolute residuals of the fixed-length sampling data sequence, similarly to [110,111].

4.4. Parameter Extraction with Impedance Spectroscopy

Despite the extra hardware testing requirement of the EIS-based models, they can give impedance characterization with the physical meaning of the properties of the materials due to the equally considered, wide frequency range applied to the cells. Compared to the limitation of the pulse current method on the sampling rate and the corresponding frequencies that can be determined during the fitting process [112], impedance results with EIS give analytical in-sight of the individual generated resistances at specific states and temperatures, by relating frequency to the respective processes.

In [113], a hybrid characterization procedure is used to model the dynamic behavior of the cell by combining information form the EIS and HPPC responses on SoC, temperature, and current dependencies. The simulated behavior of the LFP 1.2 Ah prismatic cell is adapted according to the BVE, by applying to the model correction factors generated from the differences between the simulated and the experimental voltages, approach that is also examined in [114]. The proposed model achieved a low relative error, tested with a dynamic pulse current and an application specific field-measured profile for frequency regulation purposes. A similar approach that uses EIS and pulse current excitation takes place in [72]. The authors use the impedance spectra to investigate the high-frequency Ohmic, charge-transfer and SEI resistances, while the low-frequency diffusion processes, the corresponding resistances and the overpotentials are characterized by HPPC, as an attempt to overcome the EIS challenges on modeling them. Hereafter, a static model is proposed with focus on the analysis and identification of the most dominant loss mechanisms. In particular, in short pulses (time-constant in range of seconds) overvoltages related to high-frequency components have major importance with approximately 85% on the overall losses, whereas in longer periods (min or hours range) diffusion overpotential is fully built up and equally restricts the performance of the cell. Further detailed analysis on the conduction phenomena occurring in Li-ions and modeling approaches of the diffusions can be found in [61,115].

Also, in [116], authors propose seven impedance-based ECMs with a current dependency described by the BVE. The models are tested in a model-in-the-loop environment using real vehicle data obtained in an EV prototype and current pulse tests. Temperature, calendar/cycle ageing as well as C-rate dependences are investigated on the proposed models to assess the state of available power capability of the cells at various SoCs. Results have shown a good voltage performance of the 3rd order CPE model with its accuracy being slightly dropped for either aged or operating close to the SoA limits.

Nevertheless, modeling with EIS raises practical challenges for on-board equipment integration and performance at a multi-cell topology level, while the obtained impedance in this study works as a benchmark to compare results acquired from the other numerical methods.

4.5. Parameter Extraction with Kalman Filters Based Techniques

A Kalman filter-based parameter identification has been used in [117] for a 1st order (R-R//C) ECM to assess the modeling accuracy on state of available power, when the BVE non-linear charge-transfer resistance on the current dependency is considered. The results shown a significant improvement on the estimation accuracy compared to the case that charge-transfer resistance is linear and the BVE is neglected. However, as highlighted in [48] assumption made on the constancy of the symmetry factors and the exchange current density over the lifetime and temperature can affect the accuracy estimation in the various conditions. Same authors in [10] incorporate the Arrhenius equation to evaluate the KF accuracy on an LFP when temperature effects on the redox reactions at the electrodes are considered signifying its importance.

Furthermore, Kalman filter methods can combine the parameter identification and the state estimation resulting in a system identification approach. The linear barrier of the KF method is surpassed with the Extended KF (EKF) [18], composed of first-order Taylor-series expansions that are used to linearize the non-linear time-invariant Li-ion model. For this purpose dual (DKF) or joint (JKF) Kalman filters may be used by either working in parallel and providing each other information, or by enlarging the model matrices in order to establish higher reliability with the penalty of proportionally increased computational time [118–122].

Nejad et al. [19], proposed a dual-EKF approach which combines state and weight filter for SoC and parameter identification, respectively. Both filters can simultaneously operate and feed each other to enhance stability and improve the accuracy. The filters are evaluated on ten ECMs from simple combined model up to 2nd order ECM with hysteresis. The authors conclude that for NMC cells the DP ECM is the optimal choice for ECM parametrization offering the best trade-off between performance and complexity, with RMSE < 10 mV and SoC accuracy with less than RMSE $< 1\%$ under various operation temperatures. Alternatively, the one-RC model with hysteresis can be a compromise for chemistries with higher hysteresis effect, as in LFPs.

Table 4. Comparison of several referenced works based on various electrical models and parameter identification techniques.

Refs.	Parameterization /SoC	Covering Aspects	Methodology	Conclusion
A. Analytical equations (TD)				
[75]	CC	Analytical time-domain characterization of the DP ECM.	A 40 Ah NMC cell is tested in a 7s1p module design.	The model is validated on a real-life heavy-duty application profile and found a voltage MAPE [1] $< 0.2\%$
B. Least-square methods (LS)				
[89,90]	CC/KF	RLS with an optimal forgetting factor to characterize several ECMs.	The former compares 7 ECMs, assessed with DST [5] and FUDS [6] profiles and the latter work compares 2 ECMS for 3 chemistries with DDPT [7] and WLTC [8].	The DP models shows the best performance for both works with RMSE [2] < 25 mV, and MAE [3] < 10 mV, respectively.
[86]	KF	An NLS technique is used to characterize the DP ECM of the battery cell.	A DST is performed for the 14 Ah LFP/C pouch cell. Discussion on the resistance behavior over high current profiles and SoC estimation with EKF.	An RMSE < 12 mV between the estimated and the measured voltage is observed.
[81]	CC	The DP EMC is characterized decoupled WRLS method and validated on a motorway-drive data.	A commercial 3 Ah 18650 cylindrical cell is tested in terms of SoC estimation accuracy.	An RMSE < 10 mV with the DWLS with better accuracy on both parameter and SoC identification.
C. Heuristic algorithms (GA/PSO)				
[94]	CC	MPSO method to parameterize the ECMs.	12 different ECMS are compared for cylindrical NMC and LFP cells.	A maximum RMSE < 30 mV with a DST and FUDS validation profile is observed- lowest for one ECM with hysteresis (LFP) block.
[85]	CC/KF	GA method to parameterize the five proposed ECMs for an LMO battery module.	A DST is applied to assess the accuracy of the models with CC. A FUDS validation profile the KF.	A MAE < 50 mV for the DP model is obtained with CC.
[11]	CC	A comparative study based on various heuristic algorithms for nine different ECMs.	A pouch 32.5 Ah NMC battery cell is validated with NEDC profile.	A relationship on the model-to-algorithm complexity is proposed. PSO with an RMSE < 25 mV
[96]	KF	A comparative study based on GA of 11 different ECMs and a proposed SoC estimation.	A pouch 32.5 Ah NMC battery cell is validated with NEDC [9] profile.	The 2RC is the best among all in terms of accuracy with RMSE < 5 mV.
[97]	CC	SVM, DP, SPM and combined model are parameterized with GA.	An LFP 10 Ah cell is validated with NEDC to assess the complexity versus accuracy.	Dual-Polarization order ECM is found as a good modeling trade-off.
D. Impedance spectroscopy (EIS)				
[113]	CC	A hybrid procedure for 2nd order CPE circuit is developed from EIS and HPPC tests.	A pulse test and a frequency regulation validation profile is used on a prismatic LFP/C battery cell.	A max voltage relative error $<5\%$ is observed for both profiles.
[116]	10%	Seven impedance-based ECMs with RC and CPE elements are characterized by current dependency based on BVE	NMC, LTO and LFP cells are tested in regards to state estimation.	The 3-CPE shows accurate result with an RMSE < 20 mV, but the accuracy of the models is highly dependent on the operating conditions and SoH.

Table 4. *Cont.*

Refs.	Parameterization /SoC	Covering Aspects	Methodology	Conclusion
E. Other methods (KF-based)				
[87]	KF	A three ECMs comparative study (Thevenin, PNGV, and DP) with an EKF-Ah SoC estimation algorithm.	NMC/G pouch 35 Ah cell is modeled and tested with a CCD [10] and DST to estimate the influence of each model's accuracy with the selected SoC estimation.	Best case for RMSE < 20 mV and RMSE < 15 mV for the DP model under the CCD and DST respectively
[19]	KF	A comparative study on ten ECMs that are parameterized with the dual-EKF technique.	LFP and NMC cells are validated with the NEDC profile. Focus laid on the state estimation (SoC-SoP) with erroneous initial conditions.	The DP model is chosen for having the best performance with less complexity when the hysteresis of the cells can be neglected with RMSE < 10 mV.
Proposed paper	CC	A DP ECM is proposed and characterized by analytical equations (TD), LS and heuristic optimization techniques (GA and PSO). Impedance behavior is estimated and compared to EIS.	A WLTC urban/suburban and heavy-duty current profiles are performed for LTO and NMC battery cells. Discussion of the Ohmic, total and internal resistance behavior in time and frequency.	A max RE [4] < 4% for all techniques is observed. PSO and NLS are optimal identification methods. Trade-off between accuracy, robustness and computational time set PSO as the best approach.

[1] MAPE: mean absolute percentage error. [2] RMSE: root mean square error. [3] MAE: mean absolute error. [4] RE: relative error. [5] DST: dynamic stress test. [6] FUDS: federal urban driving schedule. [7] DDPT: dynamic discharge pulse test. [8] WLTC: worldwide harmonized light vehicles test cycle. [9] NEDC: new European driving cycle. [10] CCD: constant current discharge.

5. Results, Validations and Discussions

5.1. Resistance and Power Capability

5.1.1. Lower Time-Constant Resistances

Ion concentration at the electrode-electrolyte interface builds up as the applied current pulse period is increased which creates further increment on the total resistance and the overpotential between the operating and the open circuit voltage. For a short period, impedance of the cells is kept low as the ion concentration and the diffusion overpotential are not quite developed. This -material and temperature- dependent result is illustrated for both battery cells in Figure 11.

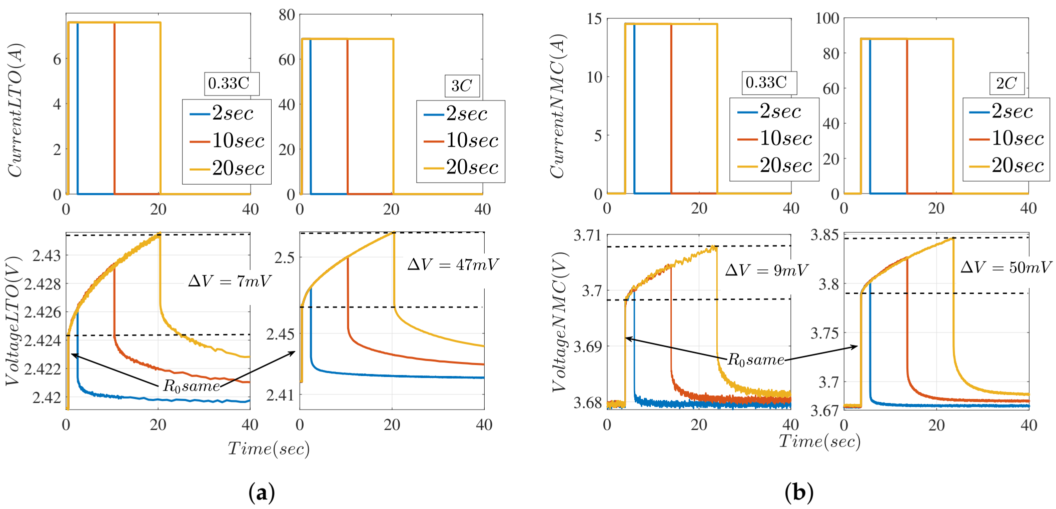

Figure 11. Experimental current pulses and generated voltage responses for (**a**) LTO and (**b**) NMC battery cells with $f_{sample} = 100$ Hz.

It is observed that regardless SoC, current amplitude/direction and pulse duration the LTO produces relatively lower polarization overpotentials compared to NMC cell (around 3 mV for short and around 7 mV for higher pulses considering measurement error of 1.5 mV, cells connectors and cables are considered to have the same impedance). Nevertheless, for the LTO cell this polarization drop refers to an approximately 50% contribution of the total 100 mV overpotential taking place for a 20 s pulse (at 3 C). For the same conditions but a current rate of 2 C, an approximately 30% contribution on the overall 180 mV polarization is observed for the prismatic NMC. That means, this NMC cell has significantly higher Ohmic, kinetics and mass transport limitations compared to the LTO at the 25 °C, which makes the former more suitable for high-energy applications, whereas the latter might be more efficient for high-power demanding applications.

If the Ohmic part is subtracted during the applied current, the effects of electrochemical charge-transfer, double layer and diffusion in electrolyte and electrodes are observed without however being possible to clearly distinguish them. Regarding this, the higher frequency processes can be separated from the EIS whereas the overvoltage build-up due to slower processes, can be roughly observed here, while the current is still flowing through the cells, or after removing the applied potential and letting the batteries reach equilibrium, as proposed from Gantenbein et al. [72]. Diffusion overpotential becomes more pronounced at decreased temperatures [50] or increased current rates [28]. On the contrary, despite the Li-ion's chemical composition Ohmic resistance expresses the inherited resistivity of the materials that hinders the charge-transferring and it is affected by SoC, temperature and lifetime [67]. Hence, the irreversible Joule losses contribution of the Ohmic resistance is the same regardless length of the pulse.

5.1.2. Total Resistances

The speed of the redox reactions which are taking place in the electrodes and convert chemical to/from electrical energy, the corresponding electrode kinetics, the diffusion coefficient and the mass transports define the power capability of the cells, whereas the applied current is an expression that defines the speed of the reactions at a certain rate [123]. The power capability $P_{pulse}|_{\Delta t}$, the total resistance R_{DC} and the corresponding overpotential ΔV_{DC} are obtained from Equations (3) and (4) with the assumption that both Ohmic and polarization processes are included in these results. As described in Equation (6), the current exchange and the symmetry factors can be further obtained. The impedance behaviors at the various current rates are plotted in Figure 12.

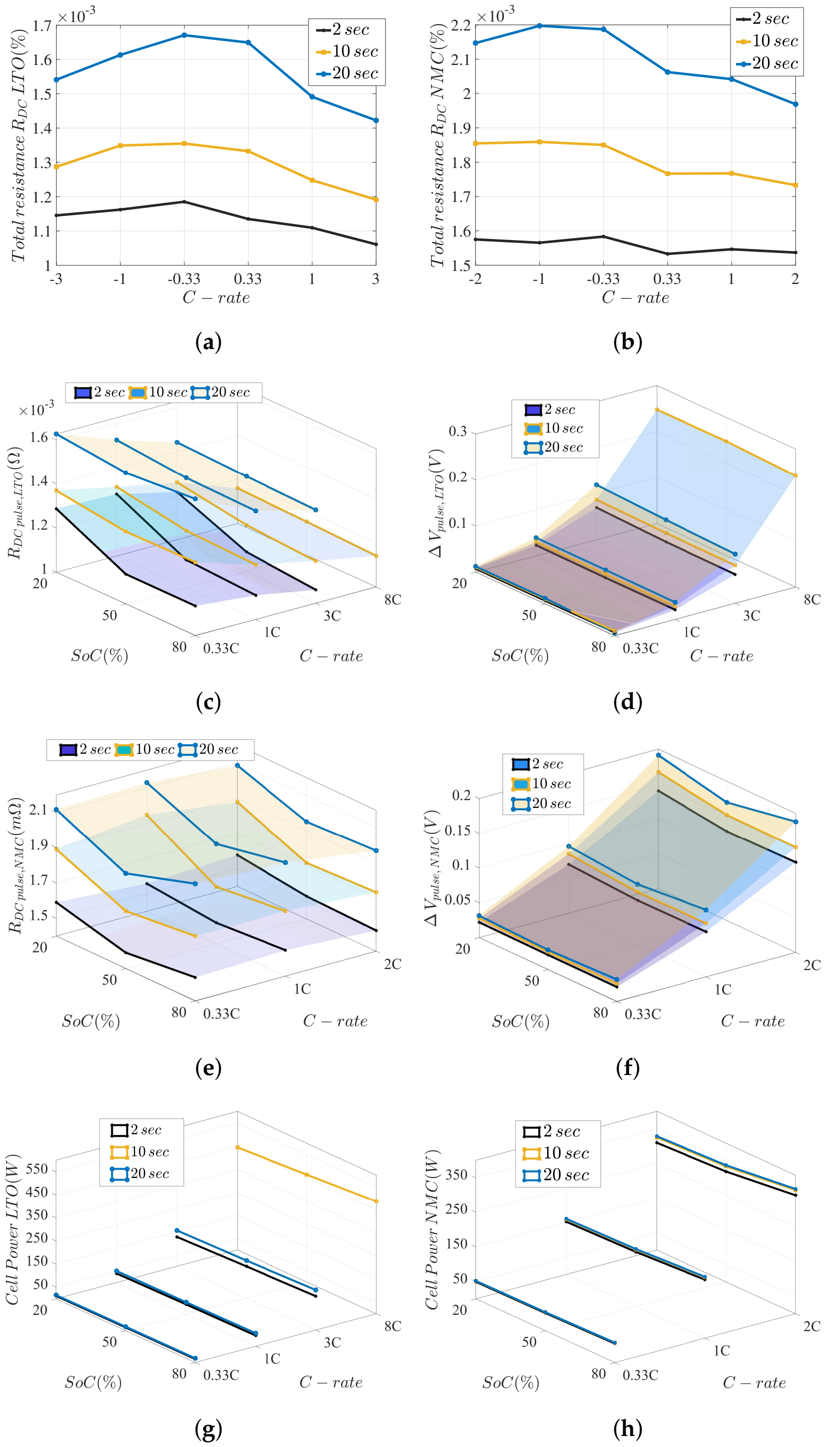

Figure 12. Total resistance at 50% SoC for (**a**) LTO and (**b**) NMC. Total charge resistance at various SoC for (**c**) LTO and (**e**) NMC. Generated exponential overvoltage for the R_{DC} for (**d**) LTO and (**f**) NMC. Pulse power capabilities of the cells at 25 °C, three different C-rates, SoCs and pulse lengths (**g**) LTO and (**h**) NMC.

By increasing the pulse current rate for a certain period, the kinetics of the electrochemical processes speed up due to increased temperature and results in a lower total resistance. Since the Ohmic resistance remains constant, the instantaneous IR_0 and the polarization overpotential between operating and open circuit potential are proportionally increased to the applied current. For illustrative reasons, the charge-discharge behavior is shown at 50% SoC in the 2D plots, whereas the charge is shown in the 3D plots over the various SoCs. It is observed that for 25 °C both cells show similar dynamic characteristics for charge and discharge, which makes the assumption on the symmetrical dependence on both anodic and cathodic branches of Equation (6) valid for these cells as well, while low variations in the range of 0.2 mOhms are mostly affected by the increased pulse period. As stated in [17] and also observed in similar LTO power capability studies [124] and in this work, the power capability of storing during charge is higher than delivering during discharge for both cells, and the difference increases proportionally to the current rate. For both chemistries difference lays in the range of a few Watts for current rates up to 1 C, whereas it is highly increased for the LTO at 3 C/8 C current with 25 Watts/85 Watts respectively, and for NMC at 2 C stays around 40 Watt. It can be concluded that the dynamic behavior of the LTO changes for very high current rates, where for 8 C $P_{charge}/P_{discharge} = 1.23$.

As the speed of the energy delivered is affected by the kinetics of the active materials and their interface, it is not possible to obtain the same value at different time periods and applied currents. The measured pulse power capabilities of the cells show that more energy can be transformed as the current rates and their duration increase, which are proportional to the generated overvoltage and diminish due to the total resistance (and the respective heat generation) increase. Comparing the two cells, the lower resistance and overpotential, along with the higher power and current rate capability makes the LTO more favorable for fast charging applications [13]. It should be noted here that a proportional behavior of R_{DC} to the P_{pulse} is observed which come against to what it is expected when the temperature effect is considered. As seen in [19], total resistance has a reverse proportional behavior with the temperature, as the kinetics and the diffusion coefficients are enhanced at such increase, which consequently leads to an inverse behavior of the power. However, it is possibly explained due to the fact that temperature has a greater effect on the total resistance (in the range of 10 mOhms for the LTO) which can drop the power capability remarkably. On the other hand, impedance increase during a pulse with a higher period is at a lower range and is not capable of dropping the power capability, although it comes with the simultaneous increase in the irreversible Joule losses. Precisely, the LTO at a 20 s pulse with a 3 C rate gives approximately 30 W more power than the same 2 s pulse, whereas the respective losses are 6.8 W compared to 5.18 W. For NMC a 2 C pulse for 20 s gives 20 W more power than the 2 s pulse, whereas at 50% SoC we have 14.4 W Joule loss compared to 11.3 W, respectively. On the other hand, for the same power capability (e.g., 150 W) NMC generates approximately 2 times less heat than LTO. Nonetheless, it is concluded that high-power pulses (duration and rate) applications are not optimal for the NMC cell, where LTO is more favorable and capable of feeding up to 8 C charging loads with 450 W and 35 W losses for 10 s at 50% SoC.

5.2. Current Profiles and Voltage Responses

The parameter identification of the cells in the time domain are fed to the dual-polarization ECM and the models are assessed with two different load profiles, a WLTC and a HD which can be seen in Figure 13a,b. The models take also initial SoC and temperature as input where they are set same for all cases. It can be seen that the WLTC is divided into two parts, urban and suburban profiles where compared to HD they are more aggressive during discharge, whereas HD has higher current charging rates. In the same figure the measured and the modeled voltage responses are shown for both profiles obtained for NLS method in this case. It can be observed that relative voltage error is below 3% in most cases whereas it is increased for the high discharge area of the suburban WLTC. For the NMC, the relative error of the HD profile stays low throughout the full cycle, while the inherited lower operational nominal voltage of the LTO is responsible for the higher relative error.

Other results from the parameter identifications are extracted in a similar way, whereas the relative voltage error for all the methods stays below 4%.

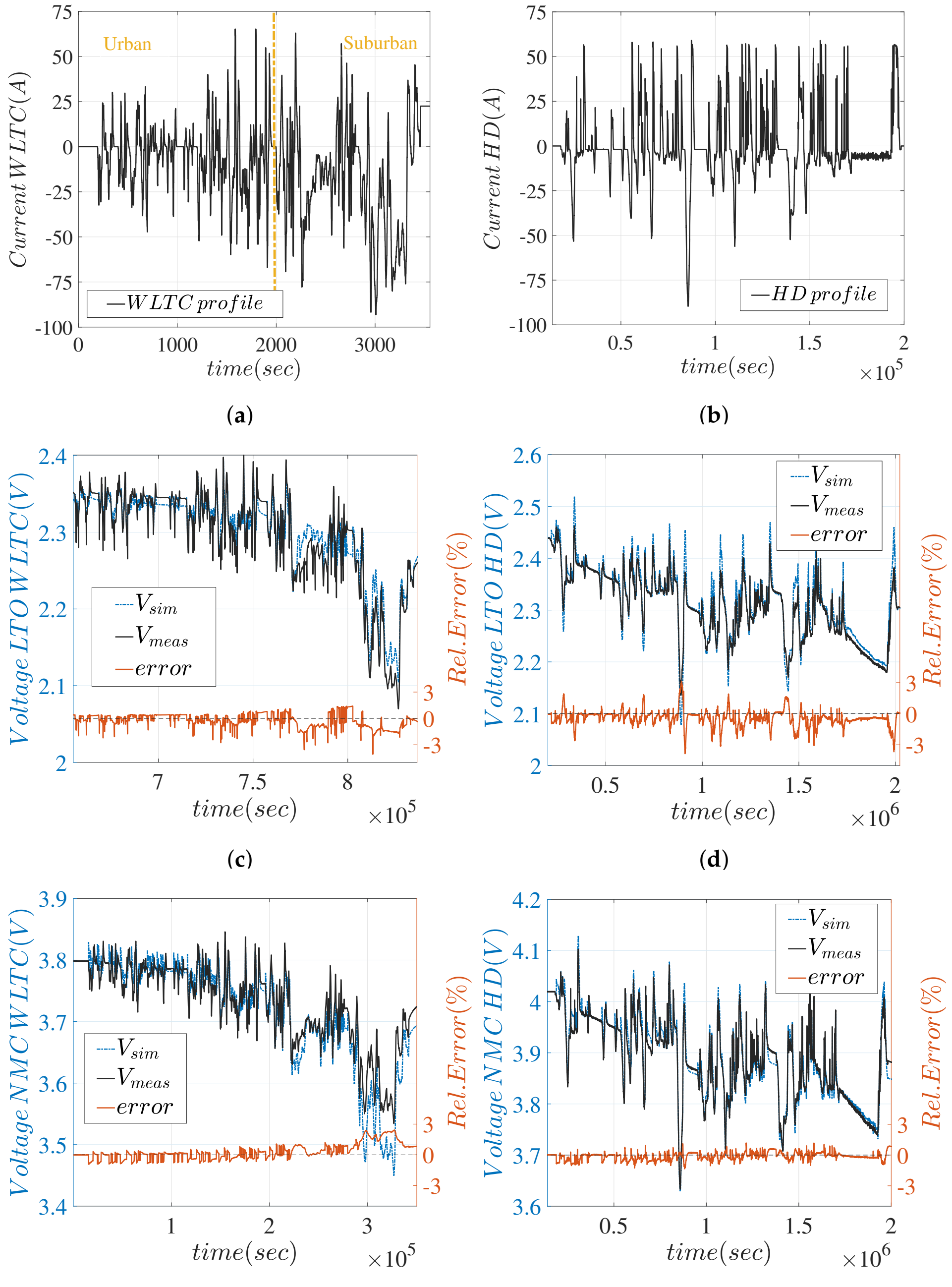

Figure 13. Characterization of LTO prismatic cell with least-square optimization at (**a**) WLTC and (**b**) HD current profile. For the same approach, LTO and NMC at WLTC (**c**,**e**) and HD (**d**,**f**) profile validation with the respective voltage relative errors in percentage.

5.3. Discussion of Methodology Robustness

This section includes a discussion of the robustness of the parameter identification methods. Since the heuristic are based on random generations and are probabilistic approaches, they can converge to the global minimum but within a range of accuracy. The robustness of the methods is investigated over ten consequent times, and the relative errors as well the RMSEs are observed. Since the PSO and the GA have shown similar robustness according to [11], and since the GA has been assessed in various research, PSO is selected here to assess the robustness over ten-time repetitive approximations. As seen in the same research, both algorithms need at least five consecutive re-identification of the parameters to produce a reduplicate voltage RMSE with a probability of 99%. On the contrary, LS and

TD do not decline from the estimation as they are derived from direct calculations and minimization of the residuals [125].

Figure 14 shows the voltage relative error and RMSEs for the PSO for ten times. It is observed that the variation of the former lays between 1% whereas the mean stays more or less the same for both cells. It is observed however that the RMSEs can deviate up to 5 mV, whereas LTO shows lower RMSE for the WLTC. NMC shows a lower mean and standard deviation for the HD profile which results in the lower RMSE compared to the WLTC.

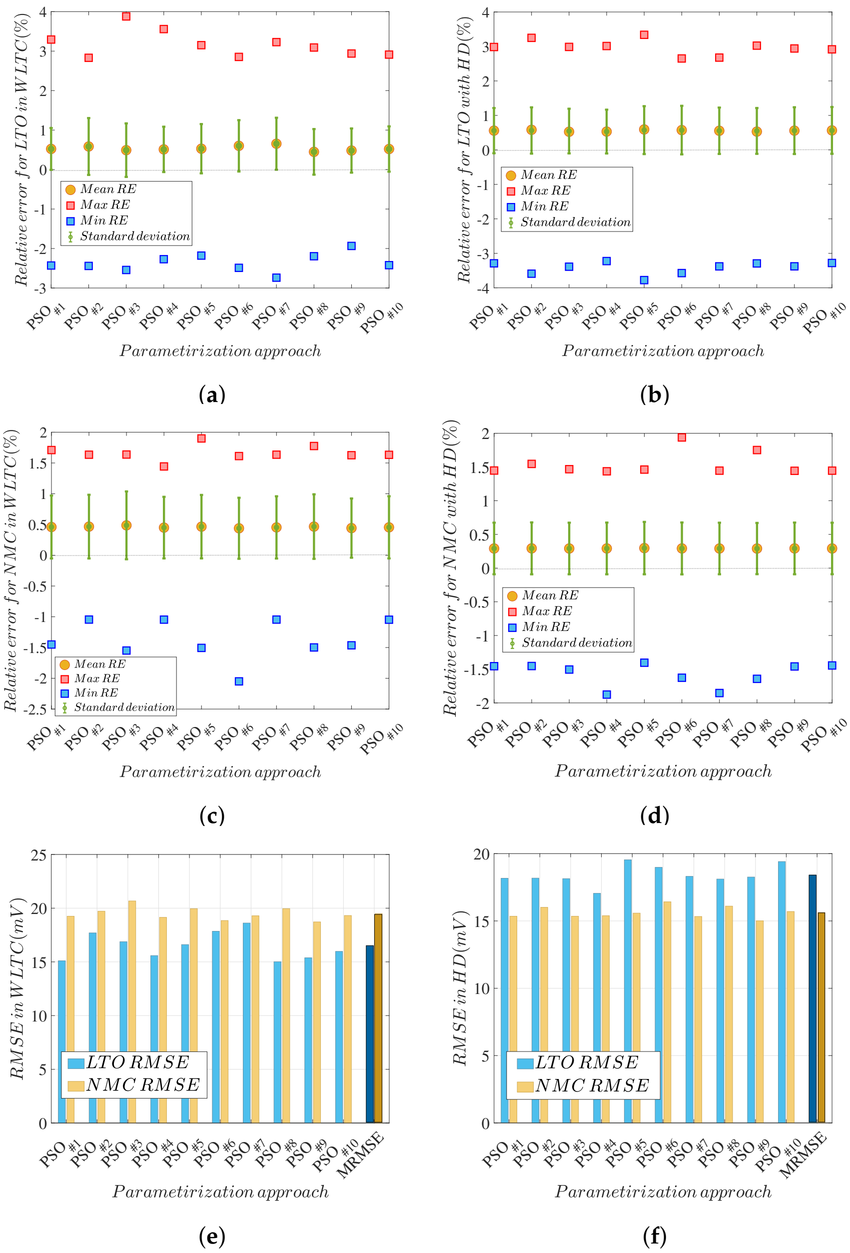

(a) (b) (c) (d) (e) (f)

Figure 14. Voltage relative error for WLTC and HD profiles for (**a**,**b**) LTO (**c**,**d**) NMC. RMSE of the ten-time consecutive PSO for WLTC (**e**) and HD (**f**) for both cells.

Robustness is seen in terms of performing the optimization algorithms for the several repetitions and estimating the deviation of the mean RMSE (M_{RMSE}) to the best fit (B_{RMSE}) as explained in Equation (10).

$$r = 1 - \frac{M_{RMSE} - B_{RMSE}}{B_{RMSE}} \tag{10}$$

Lowest voltage error for WLTC is obtained at $PSO\#8\, and\, \#9$, for HD $PSO\#4\, and\, \#9$ for the LTO and NMC. A 0.9 robustness means that the parameterization method deviates in a voltage M_{RMSE} approximately 10% from the B_{RMSE}.

The influence of the robustness depends on the accuracy of the parameter identification. The Ohmic resistance is used to compare the influence of the discrepancies, as shown in Figure 15a,b. The variations in the approximations are seen in the lower and upper SoC range where the Ohmic resistances varies approximately ΔR_0 = 0.01 mOhms. Regarding only the deviation of the R_0 it can be considered negligible, with aprx. 2% total variation. However, deviations do exist in the other parameters where total impedance, time constants and modeling V_{batt} can be affected in a higher degree. To estimate this effect, the mean internal resistance $R_{int} = R_0 + R_1 + R_2$ is calculated over the whole SoC, for each iteration of the PSO, and its deviation from the measured impedance of the EIS is assessed. The accumulative variations of R_{int} are up to 8% as it seen in Figure 15c,d for both cells.

To assess the accuracy of the PSO against the robustness the iterations are plotted from lowest to highest impedance deviation, and the respective RMSEs of the model are plotted accordingly in Figure 15e–h. However, a correlation between the lowest value of the mean internal resistance to the RMSE cannot be made, as we observe that the lowest RMSE obtained for PSO#8 for LTO under WLTC and PSO#4 under HD profile, whereas the best fit for this cell is obtained for PSO#1. On the other hand, the best fit of the NMC gives the lowest RMSEs for both WLTC and HD (PSO#9), which however is considered to be an arbitrary result. On the other hand, a proportional correlation between the RMSE and the increase of the internal resistance is observed from the curves for both cells when applying a linear regression. The positive rate of change λ denotes the degree of expected inaccuracy as the internal resistance identification trips away from the actual.

5.4. Parameter Identification Comprehensive Assessment

Taking on account the analysis performed so far, the comparison for the off-line parameter identification and the DP ECM modeling can be assessed based on the real-life loading profiles, in terms of accuracy, robustness and computational effort. First, comparisons on accuracy are performed based on the best RMSE obtained from the heuristic algorithms, the analytical approach and the least-square methods. Secondly, robustness is addressed with the deviation of the mean to the best RMSE, considering the minimum number of consecutive repetitions for achieving at least 99% model accuracy [11]. Thirdly, computational efficiency is recording the elapsed identification time of each method. In Figure 16, the relative errors of the DP ECM are shown for the two current profiles in (a) for LTO and (b) for NMC. All the methods but the TD and the GA for the HD can give absolute maximum below 4% errors for the LTO, whereas for the NMC accuracy stays above 97%. The models show good behavior for both profiles with mean relative errors below 1%. The RMSEs are shown in the subfigure (g), where the superiority in modeling accuracy of the PSO over the GA is clear for all cases. Analytical approaches are simple but difficult to catch accurately the impedance deviations and can result in higher inaccuracies. LS-based methods, on the other hand, are accurate and can be compared to the PSO approach. In (c) to (f) the normalized values of the identification methods are presented where 1 denotes the worst and 5 the best. It is seen that the WLTC loading on the LTO cell gives higher accuracy than the HD, where the inverse behavior is observed for the NMC. Robustness and computational time are not affected by the loading profile and remain the same. The scores of identification methods for all cases are shown analytically in Table 5. It is indicated that PSO has the best performance for both cells for WLTC, whereas LS is better for HD and NMC. If the robustness is considered, PSO still remains more accurate in this work whereas the computational efficiency lack is a factor of 2 from LS.

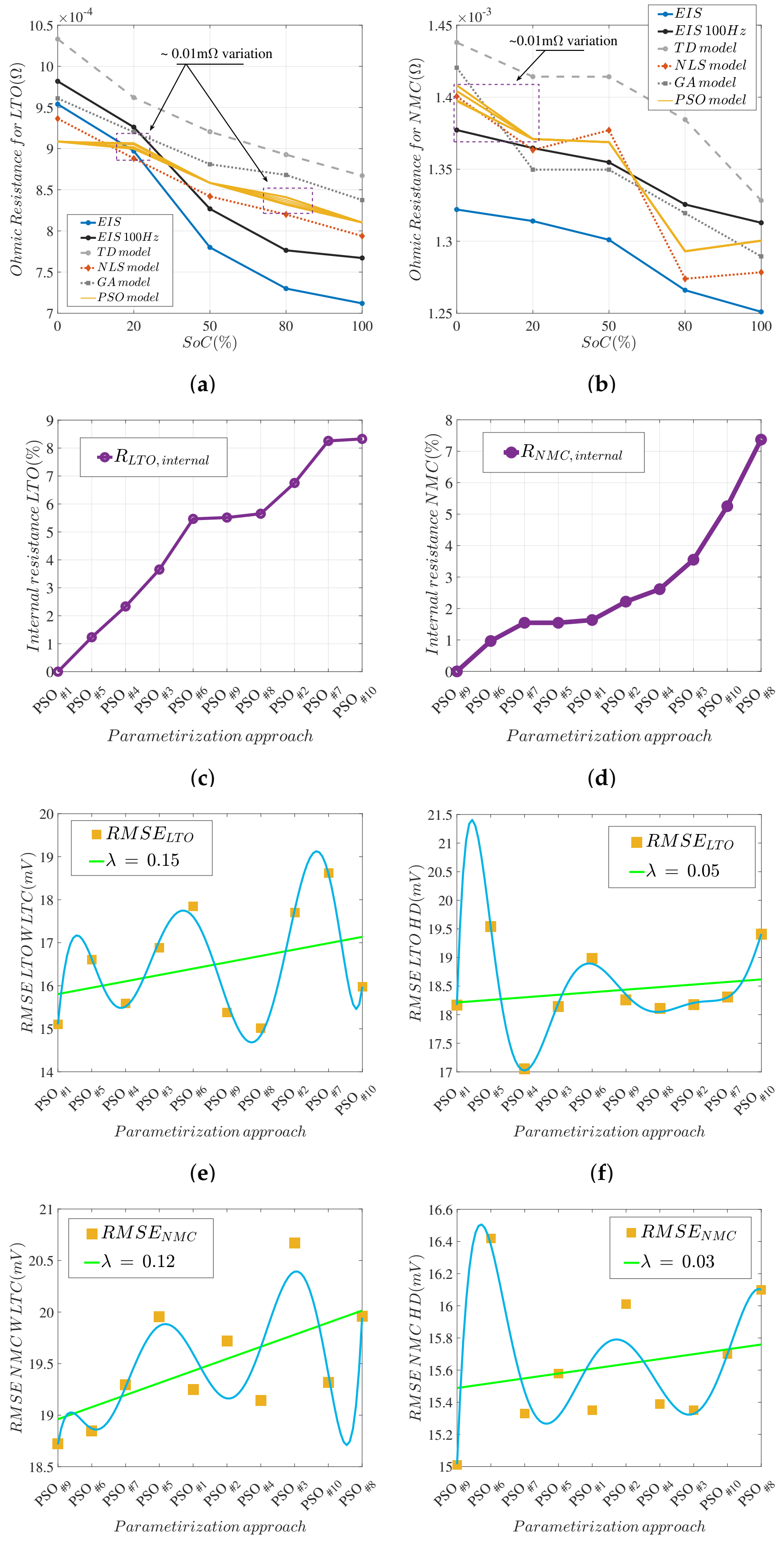

Figure 15. Ohmic resistance R_0 behavior for the different modeling approaches for (**a**) LTO and (**b**) NMC battery cells. R_{int} variation over the various PSO iterations for LTO (**c**) and NMC (**d**). Set from lowest to highest deviation from EIS. Linear regression between RMSE and PSO approach oriented according to R_{int} evolution for (**e**,**f**) LTO, (**g**,**h**) NMC.

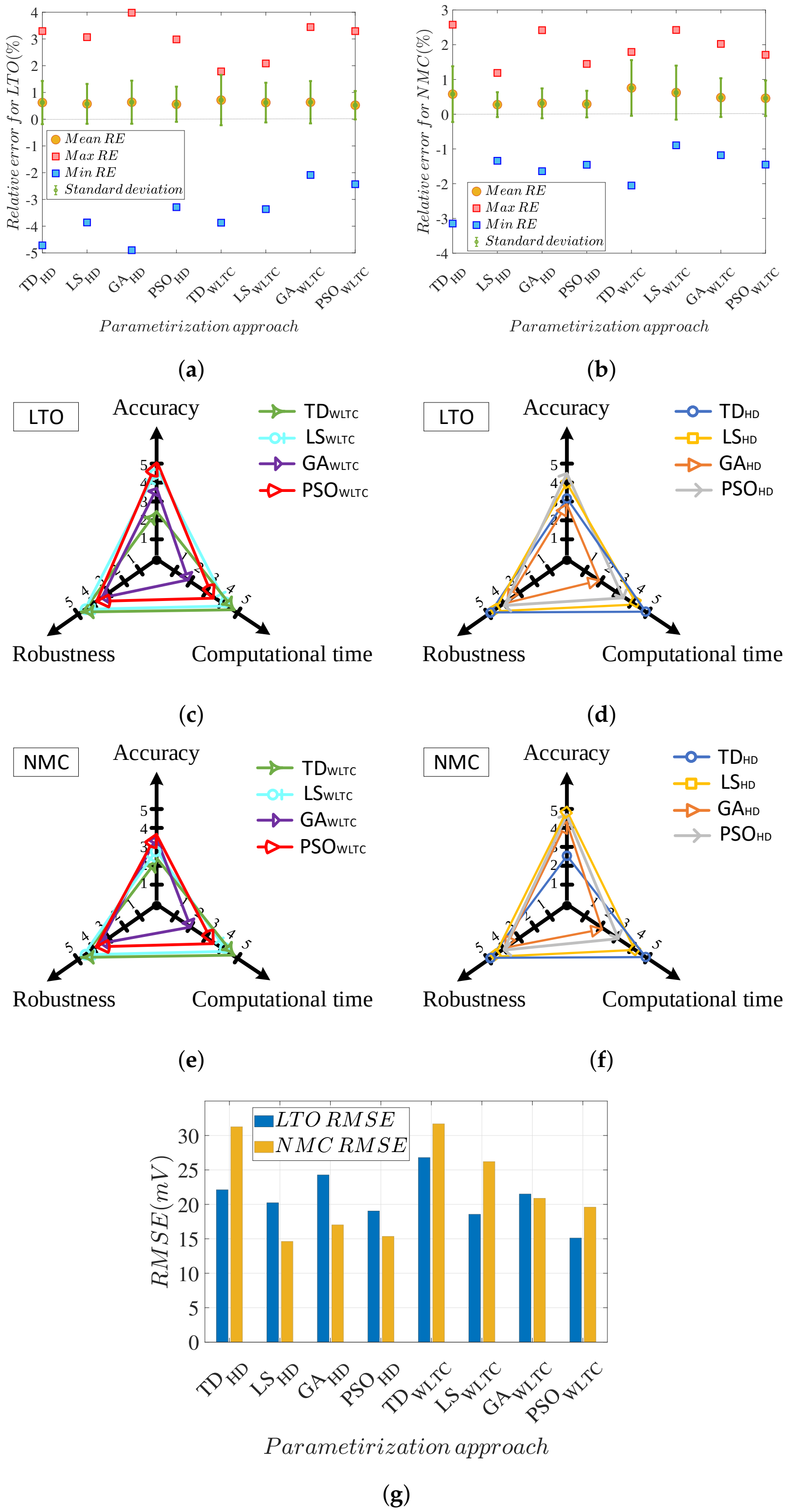

Figure 16. Statistical comparisons of the results for all the methods. Relative errors for (**a**) LTO and (**b**) NMC battery cells. For heuristic methods B_{RMSE} are taken into account and for subfigures (**c**–**f**) the mean RE is considered. In (**g**) the voltage RMSE of both cells is shown.

Table 5. Comparison of the methods.

Li-ion	Method	Mean RE (%)		Max. RE (%)		Min. RE (%)		Std. Deviation		Comp. Time (s)	Robustness (p.u)		RMSE (mV)	
		HD	WLTC	HD	WLTC	HD	WLTC	HD	WLTC	on HPPC profile	HD	WLTC	HD	WLTC
LTO	TD	0.622	0.714	3.295	1.787	4.717	3.871	0.808	0.939	<10	1	1	22.12	26.79
	LS	0.573	0.621	3.067	2.085	3.861	3.364	0.745	0.742	<60	1	1	20.22	18.56
	GA	0.635	0.634	3.982	3.444	4.899	2.086	0.805	0.791	<1200	0.90	0.87	24.27 *	21.49 *
	PSO	0.558	0.522	2.984	3.293	3.290	2.431	0.657	0.531	<100	0.92	0.90	17.05 *	15.02 *
NMC	TD	0.577	0.755	2.576	1.793	3.147	2.053	0.803	0.800	<10	1	1	31.26	31.69
	LS	0.275	0.621	1.188	2.425	1.341	0.895	0.358	0.777	<60	1	1	14.61	26.2
	GA	0.312	0.477	2.418	2.023	1.640	1.180	0.430	0.557	<900	0.94	0.94	17.02 *	20.87 *
	PSO	0.291	0.459	1.447	1.710	1.455	1.451	0.383	0.511	<100	0.95	0.95	15.01 *	18.72 *

* For the heuristic parameter identification the fit with the lowest voltage RMSE is selected.

6. Conclusions

Parameter identification methods are investigated for the DP ECM of two different anode Li-ion cells. Their nominal capacity is 23 Ah and 43 Ah respectively and they are optimal for either power or energy electromotive applications. A comprehensive research is first performed to investigate the identification methods that are used for off-line modeling. Electrical characterization methods are presented and physical investigation on the parameterization of the ECM based on frequency domain measurements is performed.

As a first step, Li-ions are experimentally tested under standardized procedures to assess their voltage to current response as well as impedance and discharge capacity capability at 25 °C. Furthermore, the hysteresis effect in both cells showed a highest value of 20 mV at the mid-SoCs, whereas it stays less than 30 mV in the high non-linear areas. For this reason, it is neglected from the dynamic modeling, for which a DP ECM approach has been followed due to its high accuracy shown in several research with an additional low computational effort. A straightforward coulomb counting method is used to estimate the SoC in the ECM, where the initial SoC has been manually adapted.

Additionally, three main parameterization methods are compared in discrete-time, with analytical equations (TD), least-square-based methods (LS) and heuristic optimization (GA and PSO). The generated models are validated with WLTC urban and suburban profiles, and a heavy-duty dynamic profile. The assessment is implemented in terms of modeling accuracy, robustness and required computational time. The modeling accuracy and the computational time are direct measurements between the simulated and the experimental voltage responses in terms of mean voltage RE and RMSE in one hand, and convergence of the parameterization method on the other. As for the robustness, it is estimated based on a 10-times repetition of the methods, where the respective variation of the ECM parameters (with focus on the Ohmic and the internal resistances) and their effect on the MREs and RMSEs are compared and showed a good agreement with most cases been less than approximately 3% and a voltage RMSE lower than 30 mV. The TD model showed the less accuracy in both. The PSO showed the lowest voltage deviations for the LTO at both loading profiles whereas for the NMC it has the best accuracy for the WLTC but not for HD. As the modeling accuracy and the robustness are concerned, PSO is the optimal approach for off-line identification. Nevertheless, work on the algorithm should be performed to reduce computational (and memory) requirements to apply the method in microcontroller and online identification.

Lastly, the Ohmic resistance obtained from the impedance spectra with EIS technique at either cross-section with real axis and at 100 Hz sampling frequency, showed a good relationship to the LS method and the heuristic algorithms. However, a comparison of the total internal resistance obtained from the PSO showed that a 0.01 mOhms variation on the Ohmic (1% to 2% depending the chemistry) and up to an accumulative 8% variation on the total internal resistance can be occur. However, the increasing RMSE of the method showed a positive correlation with that internal resistance increase and it is chemistry dependent.

Next steps may include dynamic modeling and comparisons with frequency domain on the same merits to further incorporate the physical behavior of the cells. Also, online adaptation of the PSO and the LS for state estimations investigated for several cell chemistries. A universal algorithm for parameter identification and state estimation despite Li-ion technology is also under research. Regarding the DP ECM, thermal and ageing branches are generated to thoroughly characterize the cells which are going to be presented in future work.

Author Contributions: Conceptualization, T.K., S.G., J.J.; Methodology, T.K., M.S.H., M.A.S.; Software, T.K., J.J.; Validation, T.K.; Formal Analysis, T.K.; Investigation, T.K.; Resources, L.J., G.Q., M.B., J.V.M.; Data Curation, T.K., M.S.H., M.A.S., J.J.; Writing—Original Draft Preparation, T.K.; Writing—Review and Editing, all; Visualization, T.K.; Supervision, M.B., J.V.M.; Project Administration, J.J.; Funding Acquisition, M.B., J.V.M.

Funding: This research was funded by European Union's Horizon 2020 research and innovation program under grant number 770019. This research is also part of the GEIRI project with fond number SGRIKXJSKF[2017]632.

Acknowledgments: This research has been made possible, thanks to the research project GHOST and GEIRI. This research is part of the GHOST project that has received funding from the European Union's Horizon 2020 research and innovation program under grant agreement No 770019. This research is also part of the GEIRI project with fond number SGRIKXJSKF[2017]632. Furthermore, we acknowledge Flanders Make for the support to our research team.

Conflicts of Interest: The authors declare no conflict of interest.

References

1. Nitta, N.; Wu, F.; Lee, J.T.; Yushin, G. Li-ion battery materials: Present and future. *Mater. Today* **2015**, *18*, 252–264. doi:10.1016/j.mattod.2014.10.040.
2. Zubi, G.; Dufo-López, R.; Carvalho, M.; Pasaoglu, G. The lithium-ion battery: State of the art and future perspectives. *Renew. Sustain. Energy Rev.* **2018**, *89*, 292–308. doi:10.1016/j.rser.2018.03.002.
3. Omar, N.; Daowd, M.; van den Bossche, P.; Hegazy, O.; Smekens, J.; Coosemans, T.; van Mierlo, J. Rechargeable energy storage systems for plug-in hybrid electric vehicles-assessment of electrical characteristics. *Energies* **2012**, *5*, 2952–2988. doi:10.3390/en5082952.
4. Berecibar, M.; Gandiaga, I.; Villarreal, I.; Omar, N.; Van Mierlo, J.; Van Den Bossche, P. Critical review of state of health estimation methods of Li-ion batteries for real applications. *Renew. Sustain. Energy Rev.* **2016**, *56*, 572–587. doi:10.1016/j.rser.2015.11.042.
5. Seaman, A.; Dao, T.S.; McPhee, J. A survey of mathematics-based equivalent-circuit and electrochemical battery models for hybrid and electric vehicle simulation. *J. Power Sources* **2014**, *256*, 410–423. doi:10.1016/j.jpowsour.2014.01.057.
6. Mousavi G., S.M.; Nikdel, M. Various battery models for various simulation studies and applications. *Renew. Sustain. Energy Rev.* **2014**, *32*, 477–485. doi:10.1016/j.rser.2014.01.048.
7. Grandjean, T.R.; McGordon, A.; Jennings, P.A. Structural identifiability of equivalent circuit models for li-ion batteries. *Energies* **2017**, *10*, 0–16. doi:10.3390/en10010090.
8. Huet, F. A review of impedance measurements for determination of the state-of-charge or state-of-health of secondary batteries. *J. Power Sources* **1998**, *70*, 59–69. doi:10.1016/S0378-7753(97)02665-7.
9. Buller, S.; Thele, M.; De doncker, R.; Karden, E. Supercapacitors and lithium-ion batteries for power electronic applications. *IEEE Ind. Appl. Mag.* **2005**, *11*, 62–67. doi:10.1109/mia.2005.1405828.
10. Juang, L.W.; Kollmeyer, P.J.; Jahns, T.M.; Lorenz, R.D. Improved modeling of lithium-based batteries using temperature-dependent resistance and overpotential. In Proceedings of the 2014 IEEE Transportation Electrification Conference and Expo (ITEC), Dearborn, MI, USA, 15–18 June 2014; pp. 1–8. doi:10.1109/itec.2014.6861800.
11. Lai, X.; Gao, W.; Zheng, Y.; Ouyang, M.; Li, J.; Han, X.; Zhou, L. A comparative study of global optimization methods for parameter identification of different equivalent circuit models for Li-ion batteries. *Electrochim. Acta* **2019**, *295*, 1057–1066. doi:10.1016/j.electacta.2018.11.134.
12. Brand, M.J.; Kolp, E.I.; Bach, T.; Berg, P.; Schmidt, P.; Jossen, A. Electrical resistances of soldered battery cell connections. *J. Energy Storage* **2017**, *12*, 45–54. doi:10.1016/j.est.2017.03.019.
13. Jaguemont, J.; Omar, N.; Abdel-Monem, M.; Van den Bossche, P.; Van Mierlo, J. Fast-charging investigation on high-power and high-energy density pouch cells with 3D-thermal model development. *Appl. Therm. Eng.* **2018**, *128*, 1282–1296. doi:10.1016/j.applthermaleng.2017.09.068.
14. Schweiger, H.G.; Obeidi, O.; Komesker, O.; Raschke, A.; Schiemann, M.; Zehner, C.; Gehnen, M.; Keller, M.; Birke, P. Comparison of several methods for determining the internal resistance of lithium ion cells. *Sensors* **2010**, *10*, 5604–5625. doi:10.3390/s100605604.
15. Barai, A.; Chouchelamane, G.H.; Guo, Y.; McGordon, A.; Jennings, P. A study on the impact of lithium-ion cell relaxation on electrochemical impedance spectroscopy. *J. Power Sources* **2015**, *280*, 74–80. doi:10.1016/j.jpowsour.2015.01.097.
16. Somakettarin, N.; Funaki, T. Study on Factors for Accurate Open Circuit Voltage Characterizations in Mn-Type Li-Ion Batteries. *Batteries* **2017**, *3*, 8. doi:10.3390/batteries3010008.
17. Liu, C.; Neale, Z.G.; Cao, G. Understanding electrochemical potentials of cathode materials in rechargeable batteries. *Mater. Today* **2016**, *19*, 109–123. doi:10.1016/j.mattod.2015.10.009.

18. Plett, G.L. Extended Kalman filtering for battery management systems of LiPB-based HEV battery packs—Part 2. Modeling and identification. *J. Power Sources* **2004**, *134*, 262–276. doi:10.1016/j.jpowsour.2004.02.032.
19. Nejad, S.; Gladwin, D.T.; Stone, D.A. A systematic review of lumped-parameter equivalent circuit models for real-time estimation of lithium-ion battery states. *J. Power Sources* **2016**, *316*, 183–196. doi:10.1016/j.jpowsour.2016.03.042.
20. Li, A.; Pelissier, S.; Venet, P.; Gyan, P. Fast Characterization Method for Modeling Battery Relaxation Voltage. *Batteries* **2016**, *2*, 7. doi:10.3390/batteries2020007.
21. Vetter, J.; Novák, P.; Wagner, M.R.; Veit, C.; Möller, K.C.; Besenhard, J.O.; Winter, M.; Wohlfahrt-Mehrens, M.; Vogler, C.; Hammouche, A. Ageing mechanisms in lithium-ion batteries. *J. Power Sources* **2005**, *147*, 269–281. doi:10.1016/j.jpowsour.2005.01.006.
22. Gopalakrishnan, R.; Li, Y.; Smekens, J.; Barhoum, A.; Van Assche, G.; Omar, N.; Van Mierlo, J. Electrochemical impedance spectroscopy characterization and parameterization of lithium nickel manganese cobalt oxide pouch cells: Dependency analysis of temperature and state of charge. *Ionics* **2019**, *25*, 111–123. doi:10.1007/s11581-018-2595-2.
23. Stroe, D.I.; Swierczynski, M.; Stroe, A.I.; Kaer, S.K.; Teodorescu, R. Lithium-ion battery power degradation modelling by electrochemical impedance spectroscopy. *IET Renew. Power Gener.* **2017**, *11*, 1136–1141. doi:10.1049/iet-rpg.2016.0958.
24. Maheshwari, A.; Heck, M.; Santarelli, M. Cycle aging studies of lithium nickel manganese cobalt oxide-based batteries using electrochemical impedance spectroscopy. *Electrochim. Acta* **2018**, *273*, 335–348. doi:10.1016/j.electacta.2018.04.045.
25. Eddahech, A.; Briat, O.; Bertrand, N.; Delétage, J.Y.; Vinassa, J.M. Behavior and state-of-health monitoring of Li-ion batteries using impedance spectroscopy and recurrent neural networks. *Int. J. Electr. Power Energy Syst.* **2012**, *42*, 487–494. doi:10.1016/j.ijepes.2012.04.050.
26. Zhang, Q.; Cui, N.; Shang, Y.; Duan, B.; Zhang, C. An improved Peukert battery model of nonlinear capacity considering temperature effect. *IFAC-PapersOnLine* **2018**, *51*, 665–669. doi:10.1016/j.ifacol.2018.10.154.
27. Ma, S.; Jiang, M.; Tao, P.; Song, C.; Wu, J.; Wang, J.; Deng, T.; Shang, W. Temperature effect and thermal impact in lithium-ion batteries: A review. *Prog. Nat. Sci. Mater. Int.* **2018**, *28*, 653–666. doi:10.1016/j.pnsc.2018.11.002.
28. Sauer, D. BATTERIES | Charge-Discharge Curves. In *Encyclopedia of Electrochemical Power Sources*; Elsevier: Amsterdam, The Netherlands, 2009; pp. 443–451. doi:10.1016/b978-044452745-5.00052-6.
29. Xing, Y.; He, W.; Pecht, M.; Tsui, K.L. State of charge estimation of lithium-ion batteries using the open-circuit voltage at various ambient temperatures. *Appl. Energy* **2014**, *113*, 106–115. doi:10.1016/j.apenergy.2013.07.008.
30. Tong, S.; Klein, M.P.; Park, J.W. On-line optimization of battery open circuit voltage for improved state-of-charge and state-of-health estimation. *J. Power Sources* **2015**, *293*, 416–428. doi:10.1016/j.jpowsour.2015.03.157.
31. Cuadras, A.; Kanoun, O. Soc li-ion battery monitoring with impedance spectroscopy. In Proceedings of the 2009 6th International Multi-Conference on Systems, Signals and Devices, SSD 2009, Djerba, Tunisia, 23–26 March 2009; pp. 1–5. doi:10.1109/SSD.2009.4956761.
32. Wang, X.; Wei, X.; Dai, H.; Wu, Q. State Estimation of Lithium Ion Battery Based on Electrochemical Impedance Spectroscopy with On-Board Impedance Measurement System. In Proceedings of the 2015 IEEE Vehicle Power and Propulsion Conference, VPPC 2015, Montreal, QC, Canada, 19–22 October 2015; pp. 1–5. doi:10.1109/VPPC.2015.7353021.
33. Waag, W.; Fleischer, C.; Sauer, D.U. Critical review of the methods for monitoring of lithium-ion batteries in electric and hybrid vehicles. *J. Power Sources* **2014**, *258*, 321–339. doi:10.1016/j.jpowsour.2014.02.064.
34. Lu, L.; Han, X.; Li, J.; Hua, J.; Ouyang, M. A review on the key issues for lithium-ion battery management in electric vehicles. *J. Power Sources* **2013**, *226*, 272–288. doi:10.1016/j.jpowsour.2012.10.060.
35. Zheng, Y.; Ouyang, M.; Han, X.; Lu, L.; Li, J. Investigating the error sources of the online state of charge estimation methods for lithium-ion batteries in electric vehicles. *J. Power Sources* **2018**, *377*, 161–188. doi:10.1016/j.jpowsour.2017.11.094.
36. Zhang, R.; Xia, B.; Li, B.; Cao, L.; Lai, Y.; Zheng, W.; Wang, H.; Wang, W. State of the art of lithium-ion battery SOC estimation for electrical vehicles. *Energies* **2018**, *11*, 1820. doi:10.3390/en11071820.

37. Roscher, M.A.; Sauer, D.U. Dynamic electric behavior and open-circuit-voltage modeling of LiFePO 4 -based lithium ion secondary batteries. *J. Power Sources* **2011**, *196*, 331–336. doi:10.1016/j.jpowsour.2010.06.098.
38. Dong, G.; Wei, J.; Zhang, C.; Chen, Z. Online state of charge estimation and open circuit voltage hysteresis modeling of LiFePO4 battery using invariant imbedding method. *Appl. Energy* **2016**, *162*, 163–171. doi:10.1016/j.apenergy.2015.10.092.
39. Meng, J.; Ricco, M.; Luo, G.; Swierczynski, M.; Stroe, D.I.; Stroe, A.I.; Teodorescu, R. An Overview and Comparison of Online Implementable SOC Estimation Methods for Lithium-Ion Battery. *IEEE Trans. Ind. Appl.* **2018**, *54*, 1583–1591. doi:10.1109/TIA.2017.2775179.
40. Singh, P.; Reisner, D.E.; Atwater, T.; Salkind, A.J.; Fennie, C. Determination of state-of-charge and state-of-health of batteries by fuzzy logic methodology. *J. Power Sources* **1999**, *80*, 293–300. doi:10.1016/s0378-7753(99)00079-8.
41. Bhangu, B.S.; Bentley, P.; Stone, D.A.; Bingham, C.M. Observer techniques for estimating the state-of-charge and state-of-health of VRLABs for hybrid electric vehicles. In Proceedings of the 2005 IEEE Vehicle Power and Propulsion Conference, VPPC 2005, Chicaco, IL, USA, 7–9 September 2005; pp. 780–789. doi:10.1109/VPPC.2005.1554646.
42. Guo, L.; Li, J.; Fu, Z. Lithium-ion battery SOC estimation and hardware-in-the-loop simulation based on EKF. *Energy Procedia* **2019**, *158*, 2599–2604. doi:10.1016/j.egypro.2019.02.009.
43. Chemali, E.; Kollmeyer, P.J.; Preindl, M.; Emadi, A. State-of-charge estimation of Li-ion batteries using deep neural networks: A machine learning approach. *J. Power Sources* **2018**, *400*, 242–255. doi:10.1016/j.jpowsour.2018.06.104.
44. Wu, B.; Han, S.; Shin, K.G.; Lu, W. Application of artificial neural networks in design of lithium-ion batteries. *J. Power Sources* **2018**, *395*, 128–136. doi:10.1016/j.jpowsour.2018.05.040.
45. Hansen, T.; Wang, C.J. Support vector based battery state of charge estimator. *J. Power Sources* **2005**, *141*, 351–358. doi:10.1016/j.jpowsour.2004.09.020.
46. Ng, K.S.; Moo, C.S.; Chen, Y.P.; Hsieh, Y.C. Enhanced coulomb counting method for estimating state-of-charge and state-of-health of lithium-ion batteries. *Appl. Energy* **2009**, *86*, 1506–1511. doi:10.1016/j.apenergy.2008.11.021.
47. Zhang, Y.; Song, W.; Lin, S.; Feng, Z. A novel model of the initial state of charge estimation for LiFePO 4 batteries. *J. Power Sources* **2014**, *248*, 1028–1033. doi:10.1016/j.jpowsour.2013.09.135.
48. Farmann, A.; Sauer, D.U. A comprehensive review of on-board State-of-Available-Power prediction techniques for lithium-ion batteries in electric vehicles. *J. Power Sources* **2016**, *329*, 123–137. doi:10.1016/j.jpowsour.2016.08.031.
49. Schmidt, A.; Smith, A.; Ehrenberg, H. Power capability and cyclic aging of commercial, high power lithium ion battery cells with respect to different cell designs. *J. Power Sources* **2019**, *425*, 27–38. doi:10.1016/j.jpowsour.2019.03.075.
50. Jossen, A. Fundamentals of battery dynamics. *J. Power Sources* **2006**, *154*, 530–538. doi:10.1016/j.jpowsour.2005.10.041.
51. Zhu, J.G.; Sun, Z.C.; Wei, X.Z.; Dai, H.F. A new lithium-ion battery internal temperature on-line estimate method based on electrochemical impedance spectroscopy measurement. *J. Power Sources* **2015**, *274*, 990–1004. doi:10.1016/j.jpowsour.2014.10.182.
52. Vyroubal, P.; Kazda, T. Equivalent circuit model parameters extraction for lithium ion batteries using electrochemical impedance spectroscopy. *J. Energy Storage* **2018**, *15*, 23–31. doi:10.1016/j.est.2017.10.019.
53. Andre, D.; Meiler, M.; Steiner, K.; Walz, H.; Soczka-Guth, T.; Sauer, D.U. Characterization of high-power lithium-ion batteries by electrochemical impedance spectroscopy. I: Experimental investigation. *J. Power Sources* **2011**, *196*, 5334–5341. doi:10.1016/j.jpowsour.2010.07.071.
54. Samadani, E.; Farhad, S.; Scott, W.; Mastali, M.; Gimenez, L.E.; Fowler, M.; Fraser, R.A. Empirical modeling of lithium-ion batteries based on electrochemical impedance spectroscopy tests. *Electrochim. Acta* **2015**, *160*, 169–177. doi:10.1016/j.electacta.2015.02.021.
55. Schmitt, J.; Maheshwari, A.; Heck, M.; Lux, S.; Vetter, M. Impedance change and capacity fade of lithium nickel manganese cobalt oxide-based batteries during calendar aging. *J. Power Sources* **2017**, *353*, 183–194. doi:10.1016/j.jpowsour.2017.03.090.
56. Momma, T.; Matsunaga, M.; Mukoyama, D.; Osaka, T. Ac impedance analysis of lithium ion battery under temperature control. *J. Power Sources* **2012**, *216*, 304–307. doi:10.1016/j.jpowsour.2012.05.095.

57. Do, D.V.; Forgez, C.; El Kadri Benkara, K.; Friedrich, G. Impedance observer for a Li-ion battery using Kalman filter. *IEEE Trans. Veh. Technol.* **2009**, *58*, 3930–3937. doi:10.1109/TVT.2009.2028572.
58. Liaw, B.Y.; Nagasubramanian, G.; Jungst, R.G.; Doughty, D.H. Modeling of lithium ion cells—A simple equivalent-circuit model approach. *Solid State Ionics* **2004**, *175*, 835–839. doi:10.1016/j.ssi.2004.09.049.
59. Karden, E.; Buller, S.; De Doncker, R.W. A frequency-domain approach to dynamical modeling of electrochemical power sources. *Electrochim. Acta* **2002**, *47*, 2347–2356. doi:10.1016/S0013-4686(02)00091-9.
60. Valoen, L.O.; Reimers, J.N. Transport Properties of LiPF[sub 6]-Based Li-Ion Battery Electrolytes. *J. Electrochem. Soc.* **2005**, *152*, A882. doi:10.1149/1.1872737.
61. Park, M.; Zhang, X.; Chung, M.; Less, G.B.; Sastry, A.M. A review of conduction phenomena in Li-ion batteries. *J. Power Sources* **2010**, *195*, 7904–7929. doi:10.1016/j.jpowsour.2010.06.060.
62. Mauracher, P.; Karden, E. Dynamic modelling of lead/acid batteries using impedance spectroscopy for parameter identification. *J. Power Sources* **1997**, *67*, 69–84. doi:10.1016/S0378-7753(97)02498-1.
63. Waag, W.; Käbitz, S.; Sauer, D.U. Experimental investigation of the lithium-ion battery impedance characteristic at various conditions and aging states and its influence on the application. *Appl. Energy* **2013**, *102*, 885–897. doi:10.1016/j.apenergy.2012.09.030.
64. Farmann, A.; Waag, W.; Sauer, D.U. Application-specific electrical characterization of high power batteries with lithium titanate anodes for electric vehicles. *Energy* **2016**, *112*, 294–306. doi:10.1016/j.energy.2016.06.088.
65. Waag, W.; Fleischer, C.; Sauer, D.U. On-line estimation of lithium-ion battery impedance parameters using a novel varied-parameters approach. *J. Power Sources* **2013**, *237*, 260–269. doi:10.1016/j.jpowsour.2013.03.034.
66. Zhu, J.; Knapp, M.; Darma, M.S.D.; Fang, Q.; Wang, X.; Dai, H.; Wei, X.; Ehrenberg, H. An improved electro-thermal battery model complemented by current dependent parameters for vehicular low temperature application. *Appl. Energy* **2019**, *248*, 149–161. doi:10.1016/j.apenergy.2019.04.066.
67. Reddy, T.B.; Linden, D. *Linden's Handbook of Batteries*; McGraw-Hill: New York, NY, USA, 2011; p. 2.1.
68. Fleischer, C.; Waag, W.; Heyn, H.M.; Sauer, D.U. On-line adaptive battery impedance parameter and state estimation considering physical principles in reduced order equivalent circuit battery models part 2. Parameter and state estimation. *J. Power Sources* **2014**, *262*, 457–482. doi:10.1016/j.jpowsour.2014.03.046.
69. Farmann, A.; Waag, W.; Sauer, D.U. Adaptive approach for on-board impedance parameters and voltage estimation of lithium-ion batteries in electric vehicles. *J. Power Sources* **2015**, *299*, 176–188. doi:10.1016/j.jpowsour.2015.08.087.
70. Barai, A.; Uddin, K.; Dubarry, M.; Somerville, L.; McGordon, A.; Jennings, P.; Bloom, I. A comparison of methodologies for the non-invasive characterisation of commercial Li-ion cells. *Prog. Energy Combust. Sci.* **2019**, *72*, 1–31. doi:10.1016/j.pecs.2019.01.001.
71. Wang, S.; Verbrugge, M.; Wang, J.S.; Liu, P. Power prediction from a battery state estimator that incorporates diffusion resistance. *J. Power Sources* **2012**, *214*, 399–406. doi:10.1016/j.jpowsour.2012.04.070.
72. Gantenbein, S.; Weiss, M.; Ivers-Tiffée, E. Impedance based time-domain modeling of lithium-ion batteries: Part I. *J. Power Sources* **2018**, *379*, 317–327. doi:10.1016/j.jpowsour.2018.01.043.
73. Fleischer, C.; Waag, W.; Heyn, H.M.; Sauer, D.U. On-line adaptive battery impedance parameter and state estimation considering physical principles in reduced order equivalent circuit battery models part 1. Requirements, critical review of methods and modeling. *J. Power Sources* **2014**, *260*, 276–291. doi:10.1016/j.jpowsour.2014.01.129.
74. Murashko, K.; Pyrhonen, J.; Laurila, L. Three-dimensional thermal model of a lithium ion battery for hybrid mobile working machines: Determination of the model parameters in a pouch cell. *IEEE Trans. Energy Convers.* **2013**, *28*, 335–343. doi:10.1109/TEC.2013.2255291.
75. Hentunen, A.; Lehmuspelto, T.; Suomela, J. Time-domain parameter extraction method for thévenin-equivalent circuit battery models. *IEEE Trans. Energy Convers.* **2014**, *29*, 558–566. doi:10.1109/TEC.2014.2318205.
76. Knap, V.; Stroe, D.I.; Teodorescu, R.; Swierczynski, M.; Stanciu, T. Comparison of parametrization techniques for an electrical circuit model of Lithium-Sulfur batteries. In Proceeding of the 2015 IEEE International Conference on Industrial Informatics, INDIN 2015, Cambridge, UK, 22–24 July 2015; pp. 1278–1283. doi:10.1109/INDIN.2015.7281919.
77. Stroe, A.I.; Stroe, D.I.; Swierczynski, M.; Teodorescu, R.; Kær, S.K. Lithium-Ion battery dynamic model for wide range of operating conditions. In Proceeding of the 2017 International Conference on Optimization of Electrical and Electronic Equipment, OPTIM 2017 and 2017 Intl Aegean Conference on

Electrical Machines and Power Electronics, ACEMP 2017, Brasov, Romania, 25–27 May 2017; pp. 660–666. doi:10.1109/OPTIM.2017.7975044.
78. Wang, S.; Verbrugge, M.; Wang, J.S.; Liu, P. Multi-parameter battery state estimator based on the adaptive and direct solution of the governing differential equations. *J. Power Sources* **2011**, *196*, 8735–8741. doi:10.1016/j.jpowsour.2011.06.078.
79. Xiong, R.; He, H.; Sun, F.; Zhao, K. Online estimation of peak power capability of Li-Ion batteries in electric vehicles by a hardware-in-loop approach. *Energies* **2012**, *5*, 1455–1469. doi:10.3390/en5051455.
80. Duong, V.H.; Bastawrous, H.A.; Lim, K.C.; See, K.W.; Zhang, P.; Dou, S.X. Online state of charge and model parameters estimation of the $LiFePO_4$ battery in electric vehicles using multiple adaptive forgetting factors recursive least-squares. *J. Power Sources* **2015**, *296*, 215–224. doi:10.1016/j.jpowsour.2015.07.041.
81. Zhang, C.; Allafi, W.; Dinh, Q.; Ascencio, P.; Marco, J. Online estimation of battery equivalent circuit model parameters and state of charge using decoupled least squares technique. *Energy* **2018**, *142*, 678–688. doi:10.1016/j.energy.2017.10.043.
82. Xu, J.; Mi, C.C.; Cao, B.; Cao, J. A new method to estimate the state of charge of lithium-ion batteries based on the battery impedance model. *J. Power Sources* **2013**, *233*, 277–284. doi:10.1016/j.jpowsour.2013.01.094.
83. De Sutter, L.; Firouz, Y.; De Hoog, J.; Omar, N.; Van Mierlo, J. Battery aging assessment and parametric study of lithium-ion batteries by means of a fractional differential model. *Electrochim. Acta* **2019**, *305*, 24–36. doi:10.1016/j.electacta.2019.02.104.
84. Xia, B.; Chen, C.; Tian, Y.; Wang, M.; Sun, W.; Xu, Z. State of charge estimation of lithium-ion batteries based on an improved parameter identification method. *Energy* **2015**, *90*, 1426–1434. doi:10.1016/j.energy.2015.06.095.
85. He, H.; Xiong, R.; Fan, J. Evaluation of lithium-ion battery equivalent circuit models for state of charge estimation by an experimental approach. *Energies* **2011**, *4*, 582–598. doi:10.3390/en4040582.
86. Wu, C.; Fu, R.; Xu, Z.; Chen, Y. Improved state of charge estimation for high power lithium ion batteries considering current dependence of internal resistance. *Energies* **2017**, *10*. doi:10.3390/en10101486.
87. Wang, Q.; Wang, J.; Zhao, P.; Kang, J.; Yan, F.; Du, C. Correlation between the model accuracy and model-based SOC estimation. *Electrochim. Acta* **2017**, *228*, 146–159. doi:10.1016/j.electacta.2017.01.057.
88. Zou, Y.; Hu, X.; Ma, H.; Li, S.E. Combined State of Charge and State of Health estimation over lithium-ion battery cell cycle lifespan for electric vehicles. *J. Power Sources* **2015**, *273*, 793–803. doi:10.1016/j.jpowsour.2014.09.146.
89. He, H.; Xiong, R.; Guo, H.; Li, S. Comparison study on the battery models used for the energy management of batteries in electric vehicles. *Energy Convers. Manag.* **2012**, *64*, 113–121, doi:10.1016/j.enconman.2012.04.014.
90. De Sutter, L.; Nikolian, A.; Timmermans, J.M.; Omar, N.; Van Mierlo, J. Online multi chemistry soc estimation technique using data driven battery model parameter estimation. *World Electr. Veh. J.* **2018**, *9*. doi:10.3390/wevj9020016.
91. Y., H.; Y.-Y., W. Two Time-Scaled Battery Model Identification with Application to Battery State Estimation. *IEEE Trans. Control. Syst. Technol.* **2015**, *23*, 1180–1188. doi:10.1109/TCST.2014.2358846.
92. Roscher, M.A.; Bohlen, O.S.; Sauer, D.U. Reliable state estimation of multicell Lithium-ion battery systems. *IEEE Trans. Energy Convers.* **2011**, *26*, 737–743. doi:10.1109/TEC.2011.2155657.
93. Elbeltagi, E.; Hegazy, T.; Grierson, D. Comparison among five evolutionary-based optimization algorithms. *Adv. Eng. Inform.* **2005**, *19*, 43–53. doi:10.1016/j.aei.2005.01.004.
94. Hu, X.; Li, S.; Peng, H. A comparative study of equivalent circuit models for Li-ion batteries. *J. Power Sources* **2012**, *198*, 359–367. doi:10.1016/j.jpowsour.2011.10.013.
95. Wang, Y.; Cai, Z. A hybrid multi-swarm particle swarm optimization to solve constrained optimization problems. *Front. Comput. Sci. China* **2009**, *3.1*, 38–52.
96. Lai, X.; Zheng, Y.; Sun, T. A comparative study of different equivalent circuit models for estimating state-of-charge of lithium-ion batteries. *Electrochim. Acta* **2018**, *259*, 566–577. doi:10.1016/j.electacta.2017.10.153.
97. Meng, J.; Luo, G.; Ricco, M.; Swierczynski, M.; Stroe, D.I.; Teodorescu, R. Overview of Lithium-Ion Battery Modeling Methods for State-of-Charge Estimation in Electrical Vehicles. *Appl. Sci.* **2018**, *8*, 659. doi:10.3390/app8050659.

98. Thirugnanam, K.; Ezhil Reena Joy, T.P.; Singh, M.; Kumar, P. Mathematical modeling of li-ion battery using genetic algorithm approach for V2G applications. *IEEE Trans. Energy Convers.* **2014**, *29*, 332–343. doi:10.1109/TEC.2014.2298460.
99. Blaifi, S.; Moulahoum, S.; Colak, I.; Merrouche, W. Monitoring and enhanced dynamic modeling of battery by genetic algorithm using LabVIEW applied in photovoltaic system. *Electr. Eng.* **2018**, *100*, 1021–1038. doi:10.1007/s00202-017-0567-6.
100. Fotouhi, A.; Auger, D.J.; Propp, K.; Longo, S. Accuracy Versus Simplicity in Online Battery Model Identification. *IEEE Trans. Syst. Man, Cybern. Syst.* **2018**, *48*, 195–206. doi:10.1109/TSMC.2016.2599281.
101. Hassan, R.; Cohanim, B.; Weck, O.D.; Venter, G. A Copmarison of Particle Swarm Optimization and the Genetic Algorithm. In Proceedings of the 1st AIAA Multidisciplinary Design Optimization Specialist Conference, Austin, TX, USA, 18–21 April 2005; pp. 1–13.
102. Rahman, M.A.; Anwar, S.; Izadian, A. Electrochemical model parameter identification of a lithium-ion battery using particle swarm optimization method. *J. Power Sources* **2016**, *307*, 86–97. doi:10.1016/j.jpowsour.2015.12.083.
103. Zhang, X.; Wang, Y.; Liu, C.; Chen, Z. A novel approach of battery pack state of health estimation using artificial intelligence optimization algorithm. *J. Power Sources* **2018**, *376*, 191–199. doi:10.1016/j.jpowsour.2017.11.068.
104. Dvorak, D.; Bauml, T.; Holzinger, A.; Popp, H. A Comprehensive Algorithm for Estimating Lithium-Ion Battery Parameters from Measurements. *IEEE Trans. Sustain. Energy* **2018**, *9*, 771–779. doi:10.1109/TSTE.2017.2761406.
105. Yu, Z.; Xiao, L.; Li, H.; Zhu, X.; Huai, R. Model Parameter Identification for Lithium Batteries Using the Coevolutionary Particle Swarm Optimization Method. *IEEE Trans. Ind. Electron.* **2017**, *64*, 5690–5700. doi:10.1109/TIE.2017.2677319.
106. Thomas, B.B.; Preuss, M.; Schmitt, K.; Schwefel, H.P. Challenges for Contemporary Evolutionary Algorithms. *Algorithm Eng. Rep.* **2010**, *10*, 1864–4503.
107. Deb, K.; Pratap, A.; Agarwal, S.; Meyarivan, T. A fast and elitist multiobjective genetic algorithm: NSGA-II. *IEEE Trans. Evol. Comput.* **2002**, *6*, 182–197. doi:10.1109/4235.996017.
108. Hong, Y.; Lee, C.W. Pareto fronts for multiobjective optimal design of the lithium-ion battery cell. *J. Energy Storage* **2018**, *17*, 507–514. doi:10.1016/j.est.2018.04.003.
109. Blaifi, S.; Moulahoum, S.; Colak, I.; Merrouche, W. An enhanced dynamic model of battery using genetic algorithm suitable for photovoltaic applications. *Appl. Energy* **2016**, *169*, 888–898. doi:10.1016/j.apenergy.2016.02.062.
110. Malik, A.; Zhang, Z.; Agarwal, R.K. Extraction of battery parameters using a multi-objective genetic algorithm with a non-linear circuit model. *J. Power Sources* **2014**, *259*, 76–86. doi:10.1016/j.jpowsour.2014.02.062.
111. Wang, W.; Shu-Hung Chung, H.; Zhang, J. Near-Real-Time Parameter Estimation of an Electrical Battery Model With Multiple Time Constants and SOC-Dependent Capacitance. *IEEE Trans. Power Electron.* **2014**, *29*, 5905–5920. doi:10.1109/TPEL.2014.2300143.
112. Amano, F.; Kobayashi, N. Digital Signal Processor. *J. Inst. Electr. Eng. Jpn.* **1998**, *118*, 30–33. doi:10.1541/ieejjournal.118.30.
113. Stroe, D.I.; Swierczynski, M.; Stroe, A.I.; Knudsen Kær, S. Generalized Characterization Methodology for Performance Modelling of Lithium-Ion Batteries. *Batteries* **2016**, *2*, 37. doi:10.3390/batteries2040037.
114. Andre, D.; Meiler, M.; Steiner, K.; Walz, H.; Soczka-Guth, T.; Sauer, D.U. Characterization of high-power lithium-ion batteries by electrochemical impedance spectroscopy. II: Modelling. *J. Power Sources* **2011**, *196*, 5349–5356. doi:10.1016/j.jpowsour.2010.07.071.
115. Ekstrom, H.; Fridholm, B.; Lindbergh, G. Comparison of lumped diffusion models for voltage prediction of a lithium-ion battery cell during dynamic loads. *J. Power Sources* **2018**, *402*, 296–300. doi:10.1016/j.jpowsour.2018.09.020.
116. Farmann, A.; Sauer, D.U. Comparative study of reduced order equivalent circuit models for on-board state-of-available-power prediction of lithium-ion batteries in electric vehicles. *Appl. Energy* **2018**, *225*, 1102–1122. doi:10.1016/j.apenergy.2018.05.066.

117. Juang, L.W.; Kollmeyer, P.J.; Jahns, T.M.; Lorenz, R.D. Improved nonlinear model for electrode voltage-current relationship for more consistent online battery system identification. *IEEE Trans. Ind. Appl.* **2013**, *49*, 1480–1488. doi:10.1109/TIA.2013.2253083.
118. Chiang, Y.H.; Sean, W.Y.; Ke, J.C. Online estimation of internal resistance and open-circuit voltage of lithium-ion batteries in electric vehicles. *J. Power Sources* **2011**, *196*, 3921–3932. doi:10.1016/j.jpowsour.2011.01.005.
119. Kim, J.; Lee, S.; Cho, B.H. Complementary cooperation algorithm based on DEKF combined with pattern recognition for SOC/capacity estimation and SOH prediction. *IEEE Trans. Power Electron.* **2012**, *27*, 436–451. doi:10.1109/TPEL.2011.2158554.
120. Andre, D.; Appel, C.; Soczka-Guth, T.; Sauer, D.U. Advanced mathematical methods of SOC and SOH estimation for lithium-ion batteries. *J. Power Sources* **2013**, *224*, 20–27. doi:10.1016/j.jpowsour.2012.10.001.
121. Claude, F.; Becherif, M.; Ramadan, H.S. Experimental validation for Li-ion battery modeling using Extended Kalman Filters. *Int. J. Hydrog. Energy* **2017**, *42*, 25509–25517. doi:10.1016/j.ijhydene.2017.01.123.
122. Dong, X.; Zhang, C.; Jiang, J. Evaluation of SOC estimation method based on EKF/AEKF under noise interference. *Energy Procedia* **2018**, *152*, 520–525. doi:10.1016/j.egypro.2018.09.204.
123. Berg, H. The electrochemical cell. In *Batteries for Electric Vehicles: Materials and Electrochemistry*; Cambridge University Press: Cambridge, UK, 2015; pp. 7–46. doi:10.1017/cbo9781316090978.004.
124. Stroe, A.I.; Swierczynski, M.; Stroe, D.I.; Teodorescu, R.; Kaer, S.K. Pulse Power Capability Estimation of Lithium Titanate Oxide-Based Batteries. *ECS Trans.* **2016**, *74*, 45–53. doi:10.1149/07401.0045ecst.
125. Fridholm, B.; Wik, T.; Nilsson, M. Robust recursive impedance estimation for automotive lithium-ion batteries. *J. Power Sources* **2016**, *304*, 33–41. doi:10.1016/j.jpowsour.2015.11.033.